Interfacial robustness of commercial amine-based inhibitors mitigates under-deposit corrosion of carbon steel in simulated sour conditions: A merged electrochemical and machine learning study

Eman M. Fayyad[1], Adewale K. Ipadeola[1*], Mostafa H. Sliem[1], Dana Abdeen[2], Noora Al-Qahtani[1], Ashwin RajKumar[3], Joel Jeffrey[3], Phaneendra K. Yalavarthy[3], Aboubakr M. Abdullah[1*]

[1] Center for Advanced Materials, Qatar University, Doha 2713, Qatar

[2] Qatar Shell Research and Technology Centre, P.O. Box 3747, Doha, Qatar

[3] Department of Computational and Data Sciences (CDS), Indian Institute of Science (IISc), Bangalore, India.

[*]Corresponding authors: ak.ipadeola@qu.edu.qa; bakr@qu.edu.qa

Abstract

In oil and gas industry, under-deposit corrosion (UDC) of metallic pipelines is a major problem, especially in sour environments. Not much research has been done on the effectiveness of commercial inhibitors with potent interfacial qualities in reducing UDC. In order to prevent sand (SiO_2)-induced UDC on CS in simulated sour conditions, two different commercial inhibitors, CRONOX-CRW85719 (CR1) and CRONOX-CRW85282 (CR2), were thoroughly tested over a concentration range (5 – 400 ppm). Performance was evaluated using electrochemical studies, physicochemical characterizations, and machine learning (ML) modeling. The results showed that, at optimal concentrations of 50 ppm and 200 ppm for CR1 and CR2, respectively, there were nearly total inhibition efficiencies (IE), outperforming the corrosion resistance of untreated CS. Nevertheless, after 24 h, the IEs of CR1 and CR2 were reduced by 14.7% and 4.0%, respectively, due to the presence of totally covered SiO_2 deposits on the CS surface, suggesting that deposit coverage reduces inhibitor efficacy. Because of the reduced molecular bulk and improved ability of CR2 to penetrate SiO_2 deposits, it performs better and provides better access to the metal surface relative to CR1. The random forest technique was shown to be the most appropriate predictive ML model, with an optimized mean coefficient of determination ($R^2 = 0.85 \pm 0.05$), a root mean square error (RMSE = 3.6%), and a mean absolute error (MAE = 2.7%), amongst the various machine learning models. This study emphasizes how important inhibitor molecular properties are in preventing SiO_2-induced UDC of CS in sour conditions, especially penetrating ability and strong interfacial contacts.

Keyword: Under-deposit corrosion; Carbon steel; Commercial inhibitors; SiO_2 deposit; Electrochemical techniques; Machine learning models.

1. Introduction

Under-deposit Corrosion (UDC) is a critical threat to the integrity of oil and gas facilities, due to their high corrosion kinetics, leading to a loss in mechanical properties and contribute to 20% of damage or failure in pipelines [1]. This localized corrosion is initiated underneath the precipitated sludge deposits on the pipeline metal surface with minimal flow velocity [2]. The most common pipeline sludge deposits present in oil and gas industries are barium sulfate, calcium carbonate, iron sulfide, asphaltenes, sand and other debris, which are mixed with brine containing high concentration of chloride ions with saturated acidic gases (i.e., CO_2 and H_2S) [3-5]. The precipitation of the materials breaks down the interior of the pipelines at extreme circumstances of souring of shafts/wells over time, fluid structures, pressure and temperature [6, 7]. The UDC causes localized attack and forms pits, an extremely harsh galvanic corrosion of steel occurs under the sludge deposits in the pipelines during operations [8-10]. For instance, a galvanic corrosion study in sweet conditions showed that the surfaces of mixed-deposited CS and bare CS acted as cathode and anode, respectively. The polarization of those electrodes reversed at a later stage due to the formation of corrosion product ($FeCO_3$) on the bare CS and revealed severe localized corrosion rate at the deposited CS [11]. Also, several researchers independently studied comparative corrosion properties of CS surfaces completely covered with deposits and deposit-free CS surfaces, which showed that the occurrence of UDC of CS is mainly influenced by the local operating conditions such as temperature, flow velocity, pH environment, nature and thickness of deposits [12-14], but the exact mechanism is yet unknown.

The use of potent corrosion inhibitors has proved to be the most economically viable practice to impede the internal corrosion of carbon steel, including UDC in sour conditions [15-18]. Organic compounds (OCs) with one or more hetero-atoms (N, O, P and S) are particularly potent corrosion inhibitors for preventing internal deterioration of pipelines [19-21]. The chemical nature and structural architectures of the OC-based inhibitors determine the corrosion inhibition efficiency, and applying the appropriate amount of the inhibitors leads to optimal protection of CS

surface. However, the presence of deposits reduces the tendency of OC-based inhibitors to getting adsorbed on the surface, which lowers their corrosion inhibition efficiency and eventually increases the UDC of the affected pipelines [22, 23]. For instance, a study of three imidazoline derivatives, i.e., 2-(4,5-dihydro-1H-imidazol-1-yl)ethan-1-amine (YM-1), 2-(4,5-dihydro-1H-imidazol-1-yl)ethan-1-ol (YM-2) and 1-(2-aminoethyl)-1-(2-(1-(2-aminoethyl)-2,3-dihydro-1*H*-pyrrol-1-ium-1-yl)ethyl)-4,5-digydro-1H-imidazol-1-ium chloride (YM-3), on $CaCO_3$ deposited mild steel revealed highest penetration for YM-3. On the other hand, YM-1 had the most optimized adsorption capacity of $CaCO_3$ deposit that provided the best corrosion *I.E.* of 92.3% after 16-days, due to its strong anodic dissolution with the formation of Fe-N protective layers [24]. Also, the *I.E.* of the various OC-based corrosion inhibitors (i.e., thiourea (TU), alkyl imidazoline (IM) and thiourea imidazoline (TAI)) toward SiO_2- and $CaCO_3$-deposited X65 steel demonstrated high penetration and low adsorption of TAI and TU through SiO_2- and $CaCO_3$-deposits, but both were strongly adsorbed on the X65 steel surface, due to their coordinate covalent bonds with empty d-orbitals of Fe atoms [25]. This resulted in an outstanding *I.E.* for TAI through SiO_2- (90.23%) and $CaCO_3$- deposits (96.40%) and TU (72.65%; 92.45%), unlike IM (50.49%; 57.20%) that showed strong deposits adsorption. The mechanism of UDC and hygroscopic features of ammonium salt (NH_4Cl) on CS were investigated by in-situ electrochemical tests and *ab initio* molecular dynamics (AIMD) calculations, which showed that the hygroscopic nature of NH_4Cl enabled its strong adsorption on Fe{110} facet of accumulated passive film and weak hydrogen bonding [26]. However, the hydrolysis of NH_4^+ increased H^+ ions concentration, which was the driving force for corrosion through promoting anodic adsorption and hydrogen evolution reaction (cathodic). Previous literature have confirmed the significance of molecular size, heteroatoms and chemical structure of the OC-based corrosion inhibitors on their adsorption on the surface of under-deposited carbon steel (UDCS), such that the weakly adsorbed OC-based inhibitors on UDCS exhibited relatively lower corrosion rate compared to those strongly adsorbed on UDCS [27-29]. Thus, the less adsorption and high penetration capacity of the OC-based corrosion inhibitors through deposits facilitates maximal protection of carbon steel surface. Great efforts are currently directed towards adopting the combination of two or more OC-based corrosion inhibitors with low adsorption and strong interfacial interaction, but high penetration capacity on the under-deposited carbon steel with excellent corrosion inhibition efficiency in the oil and gas industries [30-32]. However, the corrosion inhibition efficiency with robust interfacial merits of commercial

corrosion inhibitors used in the oil and gas industries for UDC is not yet reported from electrochemical perspectives and machine learning models.

The application of machine learning (ML) in corrosion science that is driven by the need to accelerate material discovery and optimize corrosion mitigation strategies is rapidly gaining traction [33, 34]. The traditional experimental and theoretical approaches to corrosion measurements are time-consuming, while ML offers the potential to analyze large datasets, identify complex patterns, and develop predictive models with improved accuracy [35]. Recent trends have demonstrated the successful implementation of ML in various corrosion related tasks such as predicting corrosion rates [36]; evaluating inhibitor performance [37]; and identifying corrosion resistance [38]. Although corrosion datasets are high quality but they often have limited samples, which lead to overfitting and poor generalizability for ML models [39]. A comprehensive review on machine learning in corrosion datasets presented model ensembles as suitable approaches for best performance prediction within corrosion datasets [34]. A prior study emphasized the importance of robust, time-dependent electrochemical data for developing machine learning models in corrosion inhibition research, like using multi-parameter modeling to determine the inhibitor efficiencies and corrosion rates [40]. For instance, Winkler *et al.* highlighted the limitations of traditional high-throughput experimentation and emphasized the role of data-driven methods for discovering effective corrosion inhibitors [41]. Pham and co-workers explored the development of quantitative structure-property relationship (QSPR)-based models for predicting the corrosion inhibition efficiency of OC-based corrosion inhibitors on CS, which demonstrated their potential for screening and developing next-generation corrosion inhibitors [42]. Aghaaminiha et al. employed machine learning to model the time-dependent corrosion rates of CS in the presence of corrosion inhibitors and revealed the accuracy of the random forest algorithm in predicting the entire time-profile of corrosion rates [43].

These studies lay the groundwork for a paradigm shift in corrosion research, where machine learning models, trained on high-quality experimental and/or computational data, guide the discovery and design of novel corrosion inhibitors. This data-driven approach promises to accelerate the development of durable, eco-friendly coatings for long-term corrosion protection, reduce maintenance costs, and streamline the design and development process. The trend of using machine learning for corrosion datasets is not just a passing fad, but a fundamental shift on how corrosion research is conducted, paving the way for a future where material design is faster, cheaper, and more efficient. Despite the advantages of ML models for corrosion research, it is yet to be studied for UDC of CS in simulated sour conditions. Hence, it is imperative to present the efficacy of the commercial corrosion inhibitors on the UDC inhibition of

CS with studied electrochemical techniques by applying different ML models. This helps to direct the attention of corrosion experts in both academia and industries towards designing new protocols for improving their performance for UDC inhibition in pipelines.

Motivated by this, corrosion inhibition efficiency of two distinct commercial inhibitors (i.e., CRONOX-CRW85719 (CR1) and CRONOX-CRW85282 (CR2)) was examined. The CR1 and CR2 were used at concentrations between 5 – 400 ppm on J55 carbon steel (CS), in the presence and absence of sand (SiO_2) deposit (full and partial coverage). The experiment was conducted in simulated sour conditions (CO_2-saturated NaCl containing sulfide ions at 60 ^oC, and 1000 rpm). An electrochemical impedance spectroscopy (EIS) and potentiodynamic polarization (PDP) testing were run for 24 h at conditions closely replicating the real-life operational conditions, particularly in the oil and gas industries. Various surface and bulk characterization techniques, including scanning electron microscopy (SEM), energy dispersive X-ray spectroscopy (EDX), X-ray diffraction (XRD), and X-ray photoelectron spectroscopy (XPS) were utilized to probe the morphology, elemental compositions, crystal structures, and surface chemistry of the pristine CS and corroded CS samples of different conditions. The electrochemical data collected from the EIS and PDP techniques were adopted as datasets and were utilized in the ML models, including random forest (RF) regressor and extreme gradient boosting (XGB) regressor, to predict the inhibition efficiency of the commercial inhibitors toward UDC of carbon steel.

2. Experimental section

2.1. Chemicals, materials and deposit preparation

All chemicals, including sodium chloride (NaCl), sodium sulfide (NaS), isopropanol (C_3H_7OH), acetone ($(CH_3)_2CO$), Nafion perfluorinated resin solution (Nafion, 5 wt.% in lower aliphatic alcohols), and carbon dioxide (CO_2) were analytical-grade reagents, procured from Sigma Aldrich (St. Louis, MO, USA). Ultra-pure water (Milli-Q system, resistivity 18.2 MX cm). Laboratory sand deposit (SiO_2, ≈ 62 μm size) was purchased from Sigma Aldrich (UK). The tested samples were J55 carbon steels (CS) of 5 mm rod shape with elemental compositions: C (0.29 wt.%), Si (0.33 wt.%), Mn (1.30 wt.%), Cr (0.06 wt.%), Mo (0.04 wt.%), S (0.001 wt.%), P (0.009 wt.%), Ni (0.02 wt.%), Cu (0.02 wt.%) and Fe (97.93 wt%). Samples were mounted in cold epoxy resin and surface area of 0.2 cm^2 was exposed to sour solutions. The CS rod surfaces were polished up

to 2000 grits. The tested CS has the elemental Prior to each corrosion test, the mounted CS rod surface was degreased with acetone and cleaned with de-ionized water. The electrolyte or test solution contained NaCl (3.5 wt.%) and Na_2S (1000 ppm). The use of Na_2S simulates the presence of H_2S and a concentration of 1000 ppm was used because the sulfide residue created on the oil and gas pipelines ranges from 200 to 500 ppm. The test solution was heated to 60°C and it was saturated with CO_2. The CS rod was mounted on conductive shaft and rotated at 1000 rpm. The two commercial inhibitors (i.e., CRONOX CRW85719 (CR1) and CRONOX CRW85282 (CR2)) were purchased from Baker Hughes: CR1 is a liquid formulation of amine salts in a glycol-aqueous solvent; meanwhile CR2 is a highly effective amine-based, film-forming corrosion inhibitor. The commercial corrosion inhibitors were used as received without further purification. The commercial corrosion inhibitors were implemented at various concentrations (5 – 400 ppm) in the sour test solution. Laboratory SiO_2 deposit was utilized to imitate the formed deposit in the pipeline, which was prepared by dispersing 300 mg of SiO_2 in a mixture of 0.6 mL isopropyl alcohol and 0.4 mL Nafion (5 wt. %), then sonicated for 2 h to achieve homogeneous mixture. A 10 μL of the prepared deposit mixture was dropped cast onto the cleaned J55 steel rod surface and dried for 2 h. Then, the deposited electrode was heated to 80 ^oC in the oven for 4 h to form a dense film of the deposit that is fully or partially covering the CS surface.

2.2 Electrochemical measurements

The corrosion measurements were carried out using GAMRY 3000 potentiostat. A three-electrode double-jacketed cell, connected to a Julabo F12 thermostat was used to maintain the solution temperature during electrochemical testing. The J55 CS rod, Ag/AgCl saturated KCl, and graphite rod served as the working electrode, reference electrode, and counter electrode, respectively. The reference electrode was placed in a lugging capillary to maintain an appropriate geometry of cell electrodes and to minimize potential and ohmic drop. A schematic representation of the experimental set-up is illustrated (Scheme 1). The experiments were done in 3.5 wt. % NaCl with 1000 ppm Na_2S added to the solution, and CO_2 purged continuously to ensure saturation with CO_2. The pH of the solution was measured to be 6.1. To realize the chemical interaction between the working electrode and electrolyte, the CS rod was inserted in the tested solution for 30 s before each measurement. After reaching open circuit potential (OCP), the EIS analysis was performed in the frequency range (0.1 Hz to 100 kHz) at a 10 mV AC amplitude [44-46]. Each EIS test was

triplicated for reproducibility. The EIS experimental data were collected, analyzed, and fitted using the suitable electrical equivalent circuits (EECs).

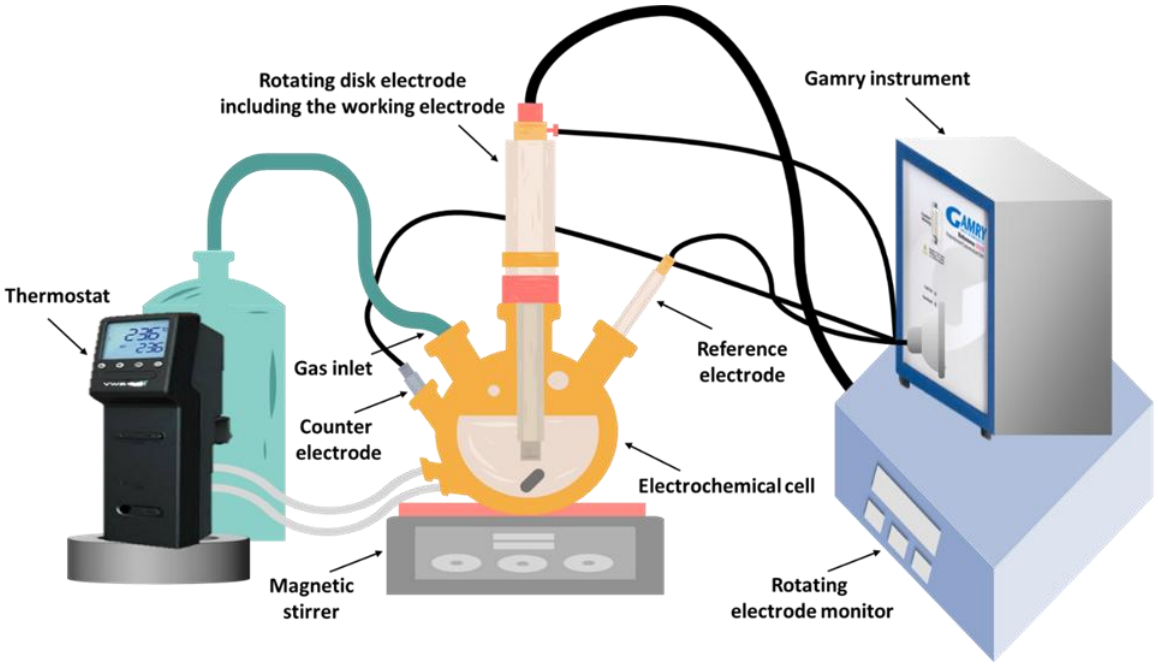

Scheme 1 The experimental set-up for electrochemical corrsoion testing of carbon steel in sour conditions.

The surface coverage (θ) and inhibition efficiency (*I.E.* %) were determined according to equations 1 and 2, respectively [47, 48].

$$\theta = \frac{R_{ct\ (inh\ CS)} - R_{ct(CS)}}{R_{ct\ (inh\ CS)}} \quad (1)$$

$$I.E.\ \% = \theta \times 100 \quad (2)$$

where $R_{ct\ (inh\ CS)}$ and $R_{ct\ (CS)}$ are the charge transfer resistances of the inhibited carbon steel and the pristine carbon steel, respectively.

Moreover, the corrosion rate (CR) in millimeters per year (mmpy) was computed using equation 3 [49, 50].

$$\mathrm{CR} = \frac{3.28\ I_{corr}\ \mathrm{M}}{\rho . n} \quad (3)$$

where CR, I_{corr}, M, ρ and n denote the corrosion rate (mmpy), corrosion current density (mA/cm^2), molar mass (M_{iron} = 56 g/mol), volume density (ρ_{iron} =7.87 g/cm^3), and quantity of electrons released during corrosion, respectively. The I_{corr} was calculated using Stern-Geary model (equation 4) [51].

$$I_{corr} = \frac{B}{R_{ct}} \text{ x } 1000 \quad (4)$$

where B and R_{ct} represent the Stern constant (0.026 V), and charge transfer resistance ($\Omega.cm^2$), respectively.

The PDP measurements were conducted in a potential range of ±250 mV vs. OCP at a scan rate of 0.30 mV/s to acquire the anodic and cathodic polarization curves. For consistency and reproducibility, every test was tripled. The corrosion inhibition efficiency (*I.E.* %) was calculated using equation 5.

$$I.E.\% = \left[\frac{i_{corr(CS)} - i_{corr(inh\ CS)}}{i_{corr(CS)}}\right] \times 100 \quad (5)$$

where $i_{corr(CS)}$ and $i_{corr(inh)}$ correspond to the corrosion current densities for the pristine CS and the inhibited CS, respectively.

Moreover, the efficiency of CRW11 corrosion inhibitor, from theoretical perspective, is measured by the inhibition power (P_{inh}), which compares the corrosion rates (CR) of inhibited and uninhibited systems, as given in equation 6.

$$P_{inh} = \log(\frac{CR_{uninh}}{CR_{inh}}) \quad (6)$$

Where CR_{uninh} and CR_{inh} are corrosion rate of uninhibited and inhibited systems, respectively.

2.3 Surface morphology and characterization

The different CS coupons are examined using different advanced surface and bulk characterization techniques. The morphologies and elemental composition of uninhibited and inhibited CS coupons, with and without SiO_2-deposit, were examined using a SEM Nova (NanoSEM 450, Thermo Fisher Scientific, Eindhoven, The Netherlands) equipped with energy-dispersive X-ray spectroscopy (EDX, Bruker detector 127 eV, Bruker, Leiderdorp, The Netherlands). Hydrophilicity and hydrophobicity of the inhibited CS with and without SiO_2-deposits was measured utilizing contact angle equipment. The XRD was employed to verify the crystalline natures and phases of pristine CS, inhibited CS and SiO_2-deposited counterparts with CR1 and CR2 inhibitors. The XPS analysis (ESCALAB 250X, ThermoFisher Scientific, Waltham, MA, USA, with AlKα excitation radiation (25W, hυ = 1486.5 eV) and 1 eV energy resolution) was conducted to probe the surface chemistry of the various CS coupons, in the presence of the corrosion inhibitors with and without SiO_2-deposits to study the adsorption of corrosion products.

2.4. Dataset construction and machine learning model development

2.4.1 Data collection and preparation

The dataset was built by combining data from two electrochemical evaluation methods, i.e., EIS and PDP. This ensured a sufficiently large dataset for robust model training. The dataset included categorical variables such as the electrochemical method used, the extent of SiO_2 deposit (partial or full coverage), and the type of corrosion inhibitor (CR1 or CR2). These were converted into numerical "one-hot vectors" to be compatible with machine learning algorithms. The final dataset consisted of 60 data points, with 30 from each electrochemical method.

2.4.2 Feature and target selection

The dataset was then divided into input features and output targets. Inhibitor efficiency (I.E.) was chosen as the output target variable, while all other variables (electrochemical method, deposit extent, inhibitor type, and other numerical measurements from EIS and PDP) served as input features.

2.4.3 Data splitting

The total dataset was split into training and testing sets using an 80/20 ratio, i.e. 80% of the data was used to train the machine learning model, and the remaining 20% was used to evaluate the model's performance on unseen data. The split was done while maintaining the same ratio of data points from each electrochemical method in both training and testing sets.

2.4.4 Model selection, evaluation and training

Since the dataset consisted of categorical and numerical data points, various regression models were explored to predict inhibitor efficiency and power. These included: Linear Regression (LR), K-Nearest Neighbor (KNN) Regression, Random Forest (RF) Regressor, Decision Tree (DT) Regressor, Gradient Boosting (GB) Regressor, and Extreme Gradient Boosting (XGB) Regressor. The performance metrics of each model were evaluated using the coefficient of determination (R^2), root mean square error (RMSE) and mean absolute error (MAE). The R^2 value measures how well the model fits the data; RMSE quantifies the average difference between the predicted and actual values; and MAE is the errors between predicted and actual inhibition efficiencies, as mathematically determined in equations 7-9.

$$R^2 = 1 - \frac{\frac{1}{m}\sum_{i=1}^{m}(|IE_{pre}^{i} - |IE_{exp}^{i}|)^2}{\frac{1}{m}\sum_{i=1}^{m}(IE_{pre}^{i} - \overline{IE})} \quad (7)$$

$$RMSE = \frac{1}{m}\sum_{i=1}^{m}(|IE_{pre}^{i} - |IE_{exp}^{i}|)^2 \quad (8)$$

$$MAE = \frac{1}{m}\sum_{i=1}^{m}(IE_{pre}^{i} - IE_{exp}^{i}) \quad (9)$$

Where IE_{pre}^{i} and IE_{exp}^{i} are predicted and experimental IE of the *i*th sample, $\overline{IE} = \frac{1}{m}\sum_{v}^{m} IE_{pre}^{i}$ is the mean value of the predicted IE.

The initial results on the training data set indicated that that the RF and XGB regressors performed well. To further assess the models and prevent overfitting (where the model performs well on training data but poorly on new data), a 4-fold cross-validation (CV) was performed to guide hyperparameter tuning. This involved splitting the data into four subsets and training the model four times, each time using a different subset as the testing and the remaining three as the training set. The test set was strictly held out and used only once for final performance evaluation.

3 Results and discussion

3.1 Electrochemical measurements

The corrosion inhibition properties of the commercial inhibitors with and without SiO_2-deposit on CS were extensively investigated utilizing sophisticated electrochemical techniques, including electrochemical impedance spectroscopy (EIS) and potentiodynamic polarization (PDP).

3.1.1 Electrochemical impedance spectroscopy

3.1.1.1 Inhibitors addition to the CS samples

To assess the corrosion inhibition capabilities of CR1 and CR2 inhibitors on CS in simulated sour conditions (i.e., CO_2-saturated 3.5 weight percent NaCl + 1000 ppm Na_2S electrolyte at 60°C under hydrodynamic conditions (1000 rpm)), EIS measurements were carried out. A concentration-dependent increase in semicircle diameter was shown by Nyquist plots for pristine CS, CS/CR1, and CS/CR2 at inhibitor concentrations (5–400 ppm) (Fig. 1(a, b)), with maximal diameters observed at 50 ppm for CS/CR1 and 200 ppm for CS/CR2. By forming adherent passive thin films through the chemisorption of CR1 and CR2 molecules on CS surface, these ideal concentrations efficiently limit the formation of corrosion products [18, 52]. In contrast, the pristine CS had a small semicircle diameter, which indicated lower R_{ct} and faster corrosion kinetics because there were no inhibitor-mediated protective layers. The experimental data were fitted using equivalent

electrical circuit (EEC) models (Fig. 1(c, d)) to measure interfacial processes, extracting parameters such as solution resistance (R_s), passive thin-film resistance (R_f), R_{ct}, double layer capacitance (C_{dl}) and passive film constant phase elements (CPE_f) (Table S1). The pristine CS showed a single capacitive loop dominated by C_{dl} and R_{ct}, which is consistent with uninhibited charge transfer at the electrode-electrolyte interface. These results highlight the effectiveness of CR1 and CR2 in regulating surface electrochemistry through adsorption-driven passivation.

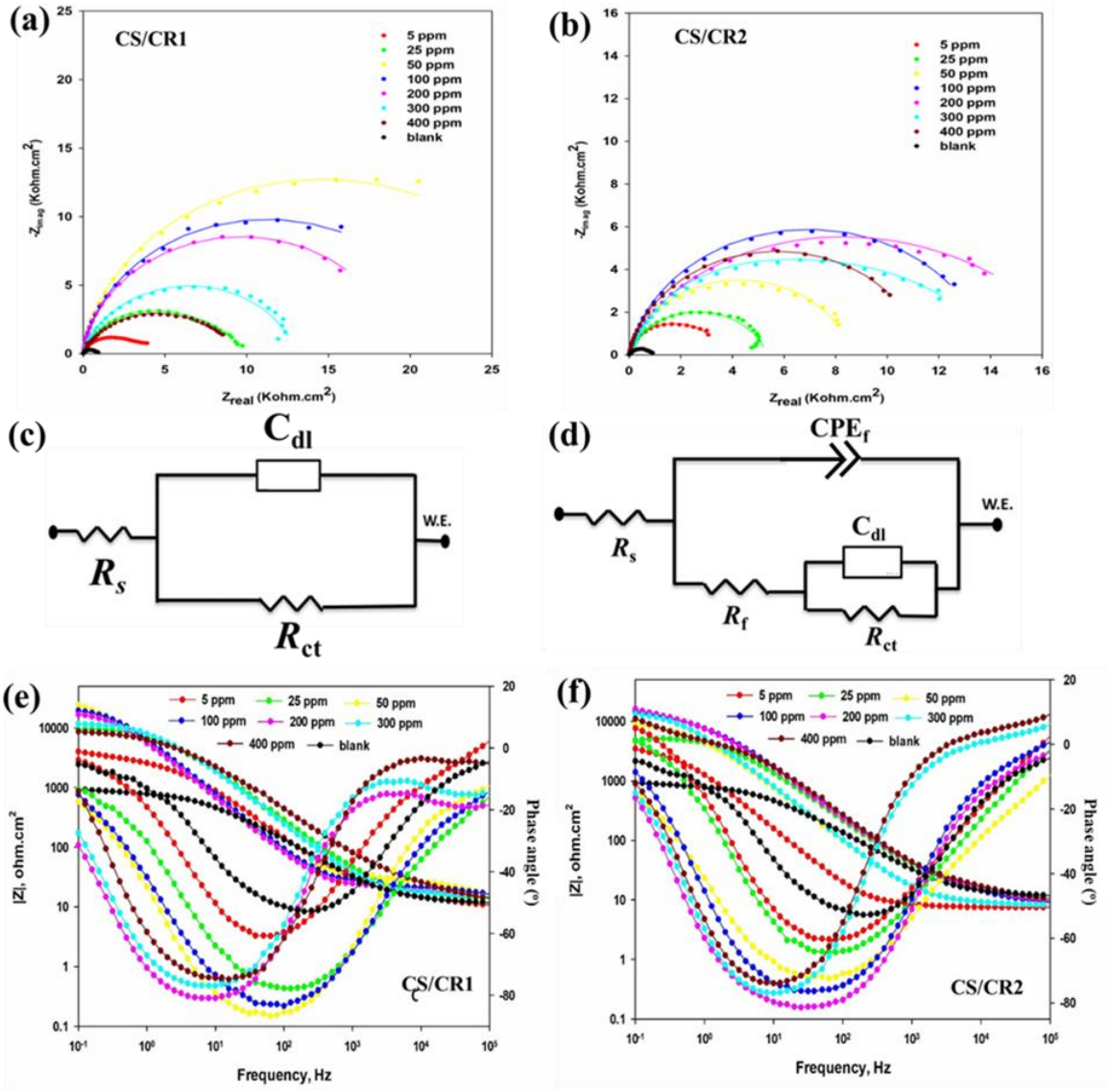

Fig. 1 (a, b) Nyquist plots, Electrical equivalent circuits (EECs) (c) one-time constant circuit, (d) two-time constants circuit, and (e, f) Bode plots of CS in sour electrolyte (3.5 wt. % NaCl + 1000 ppm Na_2S + CO_2 purging) at 1000 rpm, 60°C and different corrosion inhibitors' concentrations.

For CS/CR1 and CS/CR2, EIS study showed unique interfacial behavior. Both inhibitors showed two distinct capacitive loops in Nyquist plots, which corresponded to C_{dl} and CPE_f linked to charge transfer processes at the low-frequency region (the electrode-electrolyte interface) and the high-frequency region (the formation of an inhibitor-derived protective film). There was an increase in R_{ct} and R_f that was concentration-dependent of the inhibitors: CS/CR1 showed R_{ct} = 4980–33500 Ω·cm² and R_f = 980–6500 Ω·cm², whereas CS/CR2 showed R_{ct} = 3900–18700 Ω·cm² and R_f = 940–4460 Ω·cm². This revealed suppressed corrosion kinetics, which were significantly greater than the R_{ct} (915 Ω·cm²) for pristine CS (Fig. S1(a)). Corrosion rate (CR) measurements (Fig. S1(b)) supported the substantial mitigation of CS degradation, which is consistent with these findings. The CRs of CS/CR1 (0.01 – 0.06 mmpy) and CS/CR2 (0.02 – 0.08 mmpy) were lower than that of the uncontrolled CS substrate (0.33 mmpy). The increased corrosion inhibition efficiency of both commercial formulations in comparison to the unprotected system is demonstrated by the synergistic improvement of interfacial resistance characteristics and the corresponding decrease in CRs.

All tested concentrations showed a progressive increase in the inhibitory activity of CR1 and CR2 inhibitors, which was distinguished by noticeable interfacial covering of the pure CS surface. While CR2 showed high efficacy at 200 ppm, the CR1 inhibitor's CR attained its peak performance at 50 ppm. This discrepancy is probably caused by CR1's larger molecular bulkiness than CR2, which allows for better interfacial coverage and more efficient adsorption on the CS surface. As a result, CR1 more successfully prevents the CS substrate from making direct contact with the hostile electrolyte environment.[53]. Additionally, the EIS results showed that the CS/CR1 combination outperformed CS/CR2 in terms of high R_{ct} and low CRs, indicating improved inhibition brought on by more robust adsorption and consistent interfacial layer development. Interestingly, in inhibited samples (CS/CR1 and CS/CR2), the deformation of the Nyquist plot semi-circular arc, represented as imperfect double-layer capacitance (CPE_f) at low-frequency regions and suggested pseudo-capacitive behavior under sour circumstances. This behavior is attributed to the inhibitor coatings' induction of surface imperfections, increased roughness, and heterogeneity [54]. These results proved that CR1 and CR2 form a thin, passivating protective layer on the CS surface, imparting pseudocapacitive properties and successfully reducing corrosion processes.

The double layer capacitance (C_{dl}) presented in Table S1 was done using equation 10 [55, 56]:

$$C_{dl} = \sqrt[n]{\frac{Y_{dl}}{R_{ct}^{(n-1)}}} \quad (10)$$

In this equation, Y_{dl} represents the CPE constant applicable to the metal.

The impedance of the CPE is often defined following the power law given in equation 11.

$$Z_{\mathrm{CPE}} = \frac{1}{Y_0 (j\omega)^n} \quad (11)$$

where Y_0 stands for the CPE constant, calculated as (1/|Z|) at ω = 1 rad/s. *j* represents the imaginary number, ω denotes the angular frequency of the AC signal (1/rad), and n signifies the CPE exponent/ideality factor (range −1 to +1): when $n = 0$, the Z_{CPE} is a pure resistor; when $n = 1$, the Z_{CPE} is a pure capacitor; when $n = -1$, the Z_{CPE} is a pure inductor; and when $n = 0.5$, the Z_{CPE} is Warburg diffusion (W) [57].

The pristine CS had the lowest C_{dl} (52.6 μF·cm^{-2}), however, CS/CR1 and CS/CR2 had higher C_{dl} and CPE_f of (91.9 - 495 μF·cm^{-2} and 15.0 to 100 μS·s^n·cm^{-2}) and CS/CR2 (3.99 - 118.6 μF·cm^{-2} and 3.80 to 66.0 μS·s^n·cm^{-2}), respectively. The significantly higher C_{dl} and CPE_f values of CS/CR1 show the development of a more noticeable electrical double layer at the CS/CR1-electrolyte interface, albeit with reduced charge transfer mobility from the electrolyte to the CS substrate [58], compared to CS/CR2 and CS. This phenomenon indicates that the adsorption of CR1 and CR2 molecules onto the CS surface successfully prevents electrolyte charge carriers from entering, evidenced by the notable departure of the CPE exponent (n) values from the optimal diffusion-controlled behavior ($n = 0.5$). This observation demonstrates how well CR1 and CR2 work as corrosion inhibitors in sour environments.

Bode plot analysis showed higher overall impedance resistance for CS/CR1 and CS/CR2 at all tested concentrations in the low-frequency domain relative to pure CS, provided additional confirmation of the impedance characteristics imparted by CR1 and CR2 (Fig. 1(e, f). The CS substrate was better protected in sour solutions since the optimal surface coverage was attained at 50 ppm for CS/CR1 and 200 ppm for CS/CR2, indicating strong adsorption and interfacial layer formation at these concentrations. While the asymmetric phase angle profiles for CS/CR1 and CS/CR2 require modeling with two time-constant circuits, representing more complex interfacial processes, the symmetrical peak phase angle observed for pure CS corresponds to a single time-constant electrochemical system. Interestingly, when compared to the inhibitor-modified samples, CS showed the lowest phase angle peak magnitude and capacitive loop peak magnitude. Phase

angle peak similarities between CS/CR1 at 50 ppm and CS/CR2 at 200 ppm further support their improved capacitive behavior, which is caused by the heteroatoms and π-conjugated bonds that are a part of both molecules' chemical structures. High surface coverage values (θ) of 0.973 and 0.951 for CS/CR1 and CS/CR2, respectively, which translate to corrosion inhibition efficiency (I.E) of 97.3% and 95.1%, quantitatively support this. These results demonstrate that concentrations below 50 ppm for CR1 and 200 ppm for CR2 provide the best inhibitor performance, whereas higher concentrations may result in an excessively thick passive layer, which would reduce the effectiveness of corrosion inhibition [59, 60].

3.1.1.2 Partial SiO_2 deposit coverage with the inhibitors

The performance of CR1 and CR2 inhibitors on CS partly covered with SiO_2 deposits under simulated sour conditions over immersion periods (0–24 h) was also assessed using EIS analysis. When CR1 and CR2 inhibitors were present, Nyquist plots for CS samples with partial SiO_2 covering showed distorted semicircular arcs with widths that gradually increased with immersion duration, signifying changing interfacial characteristics (designated as CS/SiO_2(partial)/CR1 and CS/SiO_2(partial)/CR2). For CS/SiO_2(partial)/CR1, the maximum semicircle diameter was recorded at 12 h (Fig. 2(a)), while for CS/SiO_2(partial)/CR2, it was attained at 24 h (Fig. 2(b)). A distinctive double capacitive loop with related resistive elements similar to those seen in inhibitor-treated CS samples without SiO_2 deposits (CS/CR1 and CS/CR2) via EEC modeling of the EIS data. In terms of quantitative analysis, CS/SiO_2(partial)/CR1 showed R_f values (9.20 - 20.0 Ω·cm²) and R_{ct} values (1920 - 15710 Ω·cm²), peaking at 12 h, while CS/SiO_2(partial)/CR2 showed higher R_f values (2900 - 6089 Ω·cm²) and R_{ct} values (1893 - 16379 Ω·cm²), with maximum at 24 h (Table 1). These results indicate that the partial SiO_2 layer significantly hinders the diffusion of both inhibitors to the CS surface, as evidenced by significantly lower resistive parameters when compared to uninhibited samples without SiO_2 deposits. However, CR2 showed superior penetration through the porous SiO_2 layer and more effective interfacial coverage at longer exposure times, which is probably due to its less bulky molecular structure. Minimum CRs (0.02 mmpy) were observed at 12 h for CR1 and 24 h for CR2. The correlation of R_{ct} values with CRs showed that CS/SiO_2(partial)/CR1 and CS/SiO_2(partial)/CR2 displayed CRs range (0.02 – 0.16 mmpy) and (0.02 – 0.34 mmpy), respectively. These findings demonstrate that restricted CR1 and

CR2 diffusion via the SiO_2 deposit holes lowers inhibitor efficacy, making the CS surface more prone to corrosion because of decreased inhibitor interaction [61, 62].

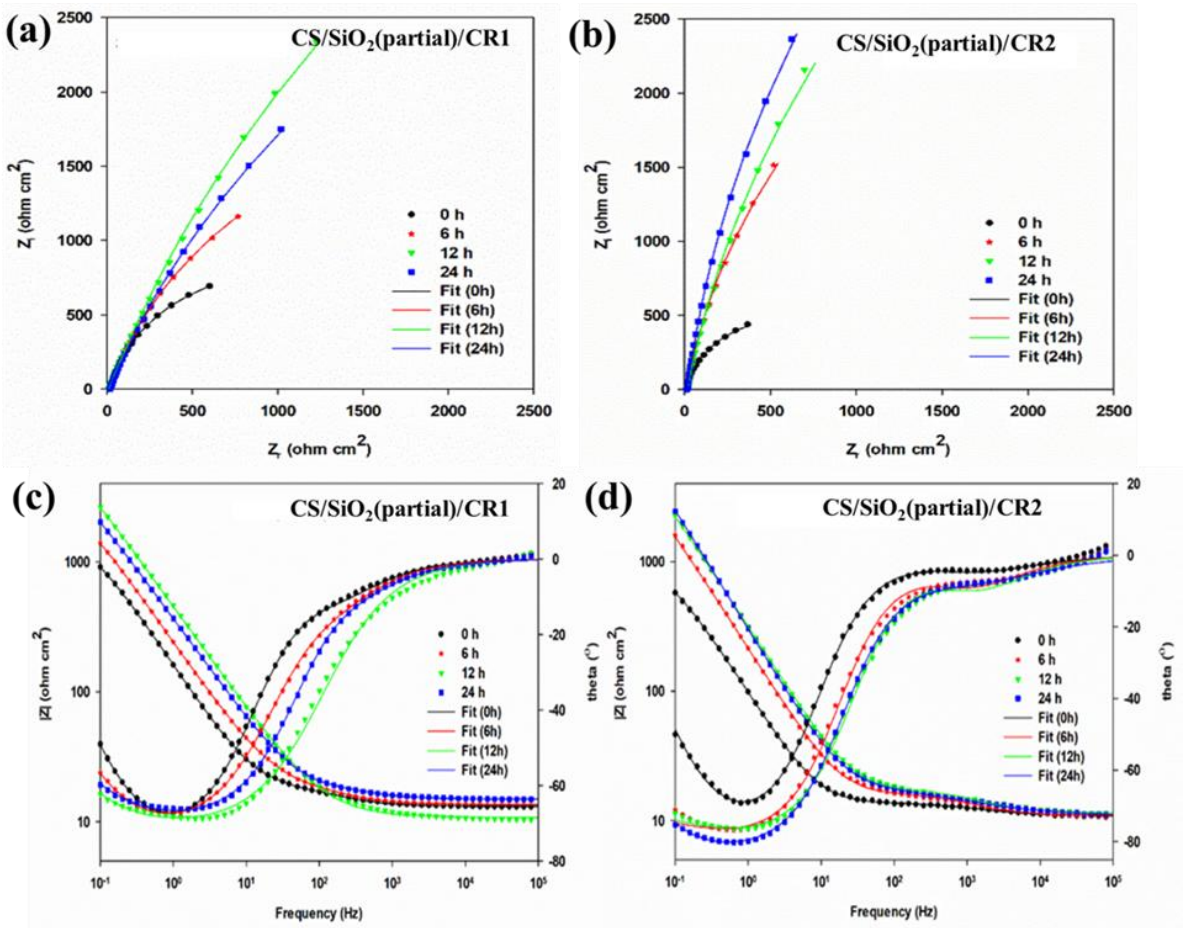

Fig. 2 (a, b) Nyquist plots and (e, f) Bode plots of CS/SiO_2(partial)/CR1 and CS/SiO_2(partial)/CR2 in sour electrolyte (3.5 wt.% NaCl + 1000 ppm Na_2S + CO_2 purging) at 1000 rpm, 60°C and different immersion times.

The capacitive and pseudocapacitive characteristics of the partially deposited SiO_2 layer on CS exhibited a decline with increasing immersion time, as summarized in Table 1. Notably, the measured C_{dl} values (55.7 - 758.0 $\mu F \cdot cm^{-2}$) and CPE_f values (406.0 - 569.0 $\mu S \cdot s^n \cdot cm^{-2}$) for the CS/$SiO_2$(partial)/CR1, whereas for CS/SiO_2(partial)/CR2, these values spanned (478.0 - 899.0 $\mu F \cdot cm^{-2}$) and (108.0 - 268.0 $\mu S \cdot s^n \cdot cm^{-2}$), respectively. The notably higher C_{dl} combined with the lower CPE_f observed in CS/SiO_2(partial)/CR2 indicates a more effective formation of the electrical double layer at the CS interface, as well as enhanced ion diffusion through the partially deposited SiO_2 layer in the CS/SiO_2(partial)/CR2-electrolyte system compared to CS/SiO_2(partial)/CR1. This

improved diffusivity is further corroborated by the ideality exponent (n_f) approaching the theoretical diffusion value (i.e., 0.5), particularly at 24 h immersion where n_f reached 0.58 for CS/SiO_2(partial)/CR2, in contrast to consistently higher values between 0.75 and 0.80 observed for CS/SiO_2(partial)/CR1 across all immersion times. These findings collectively suggest that CR2, due to its smaller particle size, achieves deeper penetration into the SiO_2 pores and establishes a more robust interfacial coverage on the CS substrate, thereby enhancing the electrochemical performance of the composite.

The Bode plots for CS/SiO_2(partial)/CR1 and CS/SiO_2(partial)/CR2 under sour conditions show that an increase in the overall resistance of CS partially covered with simulated SiO_2 deposit is correlated with a longer immersion period (Fig. 2(c, d)). This pattern is consistent with the resistive properties shown in inhibited under-deposited samples, where peak overall resistance values for CS/SiO_2(partial)/CR1 and CS/SiO_2(partial)/CR2 were reached at 12 and 24 h, respectively. According to these results, the penetration of CR1 through SiO_2 layer reached maximum after 12 h, when its adsorption onto CS surface is feasible. To maximize resistance against under-deposit corrosion (UDC), CR2 penetrates at a longer immersion time of 24 h through SiO_2 deposit, forming a strong interfacial adsorption layer. The use of a two-time constant equivalent circuit model is further supported by the asymmetrical profiles shown in the Bode curves for both inhibitors (Fig. 2(c, d)). Notably, CS/SiO_2(partial)/CR2 exhibits better capacitive behavior than CS/SiO_2(partial)/CR1 due to its larger phase angle values, which reach 90° between 6 and 24 h. This improvement is ascribed to CR2's enhanced penetration and mild adsorption, which promotes robust interfacial coverage on CS surface and successfully reduces UDC throughout prolonged immersion periods. The increasing surface coverage (θ) and inhibition efficiency (I.E.) with immersion duration support these electrochemical observations. At 12 h, CS/SiO_2(partial)/CR1 reached maximum θ and I.E. values of 0.80–0.94 (80.4–94.2%), while at 24 h, CS/SiO_2(partial)/CR2 reached 0.71–0.94 (71.2–94.4%). Significantly, samples with the partial SiO_2 deposit had lower inhibition efficiencies than samples without it, suggesting that the SiO_2 layer reduces the potency of commercial inhibitors in preventing UDC in CS.

3.1.1.3 Full SiO_2 deposit coverage with the inhibitors

The electrochemical behavior of CS) with full SiO_2 coverage in sour conditions was thoroughly examined using EIS. Deformed semicircular profiles were shown in Nyquist plots for

CS/SiO_2(full)/CR1 and CS/SiO_2(full)/CR2 at immersion times of 0–24 h (Fig. 3(a, b)), which were consistent with patterns observed for partial SiO_2 coverage. Ideal inhibitor penetration and strong interfacial adsorption through the SiO_2 matrix were shown by the maximum impedance arc diameters, which were recorded at 12 h for CR1 and 24 h for CR2. In accordance with inhibited samples (CS/CR1, CS/CR2), independent of SiO_2 coverage, EEC modeling (Fig. 1d) showed dual capacitive loops with resistive components (R_s, R_f, R_{ct}) and capacitive portion (C_{dl}, CPE_f). CR2 showed progressive resistance increases over time, but CR1 reached peaks of R_f and R_{ct} values at 12 h for full SiO_2 deposition. In contrast to the sterically inhibited CR1, this divergence indicates improved pore penetration and adsorption kinetics for CR2, most likely because of its reduced molecular weight, which permits deeper infiltration through SiO_2 pores. The findings highlight time-dependent interfacial stabilizing processes that are mediated by the integrity of the SiO_2 layer and inhibitor physicochemical characteristics.

The full SiO_2 deposition on CS exhibited diminished resistive properties, resulting in a marked decrease in the corrosion inhibition efficacy of both CR1 and CR2 inhibitors compared to partially SiO_2-deposited samples [63]. This finding substantiates the limited penetration of CR1 and CR2 through the SiO_2 layer, leading to reduced direct interaction with the CS substrate. Consequently, fully SiO_2-covered CS surfaces are more vulnerable to UDC, as evidenced by elevated CRs observed in most experimental outcomes. EIS analysis revealed that the capacitive and pseudocapacitive characteristics of fully SiO_2-deposited CS with CR1 and CR2 (CS/SiO_2(full)/CR1 and CS/SiO_2(full)/CR2) progressively declined with prolonged immersion. Notably, the CS/SiO_2(full)/CR2 demonstrated superior C_{dl} and CPE_f values, indicating enhanced interfacial charge mobility relative to CS/SiO_2(full)/CR1. This improvement is attributed to the smaller molecular size of CR2, facilitating its diffusion through SiO_2 pores and enabling robust interfacial coverage on the CS surface. Ideality factors (n) further corroborated this behavior, with CS/SiO_2(full)/CR2 exhibiting consistently lower values (0.58–0.85) across immersion times compared to CS/SiO_2(full)/CR1 (0.62–0.87).

The resistive behavior increased for 12 and 24 h, according to bode plot analysis, with CS/SiO_2(full)/CR1 and CS/SiO_2(full)/CR2, respectively exhibiting the highest resistance values (Fig. 3(c, d)). The efficacy of the bulkier CR1 molecule was diminished by diffusion limitations through the SiO_2 layer, while CR2 consistently demonstrated higher total resistance ($R_f + R_{ct}$) due to its enhanced penetration and interfacial stability, even though this trend is similar to that of

partially SiO_2-deposited CS. The phase angle plots' asymmetry, which initially displayed better capacitive behavior for CS/SiO_2(full)/CR1 but shifted in favor of CS/SiO_2(full)/CR2 at extended immersion (6–24 h), demonstrated the application of a two-time constant equivalent circuit and demonstrated CR2's improved interfacial interaction over time. Overall, as demonstrated by decreased surface coverage (θ) and inhibition effectiveness (I.E.) values, full SiO_2 coverage severely impairs the corrosion inhibition capabilities of both CR1 and CR2. At the early stages of immersion, CR1 showed especially poor inhibition, reaching peak efficiency only after 12 h, while CR2's θ and I.E. values increased progressively over the exposure time. These findings highlight how the efficiency of commercial inhibitors, particularly those based on large chemical compounds like CR1, is significantly reduced by complete SiO_2 deposition on CS.

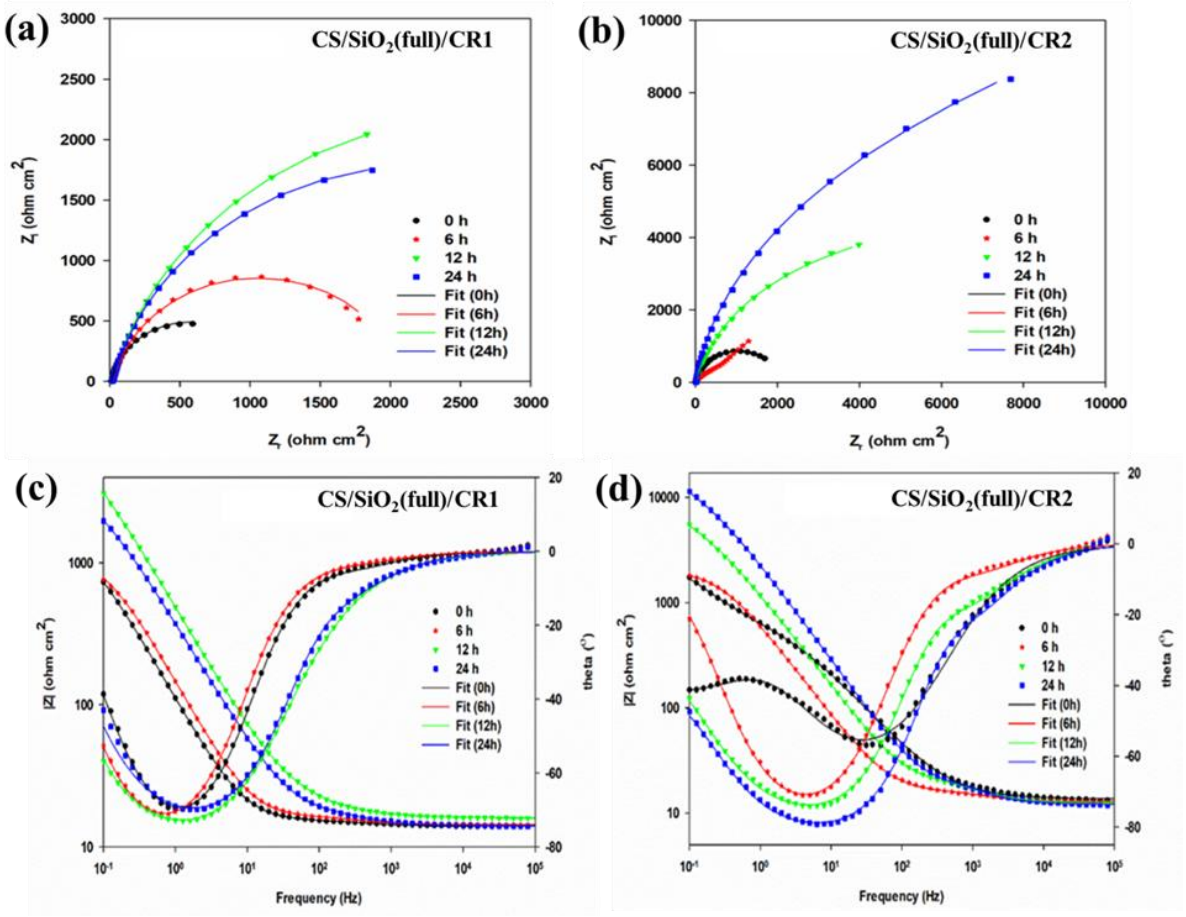

Fig. 3 (a, b) Nyquist plots and (c, d) Bode plots of CS/SiO_2(full)/CR1 and CS/SiO_2(full)/CR2 in sour electrolyte (3.5 wt.% NaCl + 1000 ppm Na_2S + CO_2 purging) at 1000 rpm, 60°C and different immersion time (0 – 24 h).

Table 1 EIS parameters obtained for simulated under-deposited carbon steel with corrosion inhibitors, including CS/SiO_2(partial)/CR1, CS/SiO_2(partial)/CR2, CS/SiO_2(full)/CR1 and CS/SiO_2(full)/CR2 in the electrolyte (3.5 wt. % NaCl + 1000 ppm Na_2S + CO_2 purging

Samples' name	Time (h)	R_f ($\Omega.cm^2$)	CPE_f		R_{ct} ($\Omega .cm^2$)	CPE_{dl}		C_{dl} ($\mu F.cm^{-2}$)	Corrosion rate (mmpy)	θ	*I.E.* (%)
			Y_f ($\mu S.s^n cm^{-2}$)	n_f		Y_{dl} ($\mu S.s^n cm^{-2}$)	n_{dl}				
CS/SiO_2(partial)/CR1	0	9.2	569	0.80	1920	727	0.89	758	0.16	0.523	52.3
	6	12.4	463	0.82	4660	464	0.82	549	0.06	0.804	80.4
	12	20.0	456	0.77	15710	56	0.96	55.7	0.02	0.942	94.2
	24	18.5	406	0.75	11290	155	1.00	155	0.03	0.919	91.9
CS/SiO_2(partial)/CR2	0	2.900	268	0.79	1893	867	0.93	899	0.34	0.517	51.7
	6	9.720	108	0.79	3180	463	0.92	478	0.10	0.712	71.2
	12	6.089	209	0.78	7090	632	0.94	695	0.04	0.871	87.1
	24	8.766	118	0.58	16370	503	0.93	589	0.02	0.944	94.4
CS/SiO_2(full)/CR1	0	3.4	552	0.86	1140	783	0.95	778	0.27	0.197	19.7
	6	7.7	77	0.86	2040	220	0.94	209	0.15	0.552	55.2
	12	27.7	2.8	0.62	9800	143	0.87	150	0.03	0.907	90.7
	24	19.3	7.2	0.87	6900	180	0.98	181	0.04	0.867	86.7
CS/SiO_2(full)/CR2	0	3.4	118	0.85	2040	188	0.92	173	0.15	0.552	55.2
	6	5.5	109	0.79	3000	186	0.84	166	0.10	0.695	69.5
	12	16.3	85	0.87	7115	160	0.96	161	0.04	0.871	87.1
	24	17.3	49	0.79	11990	130	0.98	131	0.03	0.924	92.4

3.2 Potentiodynamic polarization (PDP)

3.2.1 Inhibitors addition to the CS samples

Potentiodynamic polarization (PDP) or Tafel analysis is amongt the most efficient ways to assess the interfacial interactions and inhibition efficiencies of different commercial inhibitors toward the UDC of CS and their associated anodic and cathodic mechanisms [64]. In this study, PDP curves were obtained for pristine CS, CS/CR1 and CS/CR2, in a CO_2-saturated 3.5 wt% NaCl solution containing 1000 ppm Na_2S, at 1000 rpm and 60°C, across different inhibitors' concentrations (Fig. 4(a, b)). Corrosion performance metrics, like corrosion potential (E_{corr}), corrosion current density (i_{corr}), and anodic/cathodic Tafel slopes (b_a and b_c), were derived from these curves, and I.E. was calculated based on i_{corr} values (Table S2). Because iron dissolution has a low activation energy and interacts with CO_2 and sulfide ions, the pristine CS had the most negative E_{corr} value (-0.677 V), indicating rapid corrosion under sour conditions [55, 65]. CR1 and CR2 inhibitors, on the other hand, considerably raised the energy barrier for iron oxidation. This was demonstrated by a positive shift in E_{corr} values (-654 to -604 mV) for CS/CR1 and (-610 and -671 mV) for CS/CR2, with the greatest effects observed at 50 ppm for CS/CR1 and 200 ppm for CS/CR2 (Fig. 4(c, d)). This change is indicative of the inhibitors' adsorption and creation of a passive layer at the CS interface, which successfully prevents the production of corrosion products and delays iron oxidation in spite of the harsh surroundings [66]. The results highlight the inhibitors' ability to modify both anodic and cathodic reactions, thereby improving corrosion resistance through surface adsorption and passivation mechanisms under sour conditions. Interestingly, CS/CR1 showed more positive E_{corr} values than CS/CR2, indicating a superior protective tendency of CR1 against corrosion attack.

All investigated samples had anodic Tafel slopes (b_a) that were consistently lower than their corresponding cathodic slopes (b_c), suggesting that anodic reactions proceed more quickly than cathodic processes. This finding implies that the commercial inhibitors reduce anodic activity mainly through interactions at the CS interface. The pristine CS and the inhibited samples, CS/CR1 (73 mV) and CS/CR2 (69 mV), had different E_{corr}, although these shifts were smaller than the crucial threshold of 85 mV. This suggests that both CS/CR1 and CS/CR2 are mixed-type inhibitors that impact both anodic and cathodic reactions. The development of thin, passivating coatings with robust interfacial coverage of CR1 and CR2 inhibitors on both anodic and cathodic sites is responsible for this dual inhibition [67, 68]. As inhibitor concentration increased, the anodic and

cathodic polarization curves for CS/CR1 and CS/CR2 shifted negatively in comparison to the i_{corr} of the uninhibited CS (147.0 µA/cm²). This resulted in notable decreases in i_{corr} values (2.60 – 24.5 µA/cm²) and (6.20 – 35.0 µA/cm²) for CS/CR1 and CS/CR2, respectively. With peak performance at these optimum concentrations, the lowest i_{corr} values were recorded at 50 ppm for CS/CR1 and 200 ppm for CS/CR2, which corresponded to maximal I.E. of 98.2% and 95.8%, respectively (Fig. 4(c, d)). These results demonstrate that CR1 and CR2 inhibitors effectively adsorb onto the CS surface, with the ideal dosages for optimum corrosion protection being 50 ppm and 200 ppm. Significantly, CS/CR1 outperformed CS/CR2 in terms of inhibition efficiency at lower concentrations (up to 100 ppm), while at concentrations higher than 100 ppm, CS/CR2's inhibition efficiencies were comparable to CS/CR1. This highlights CR1's strong corrosion inhibition ability over a wide concentration range in the absence of SiO_2 deposit.

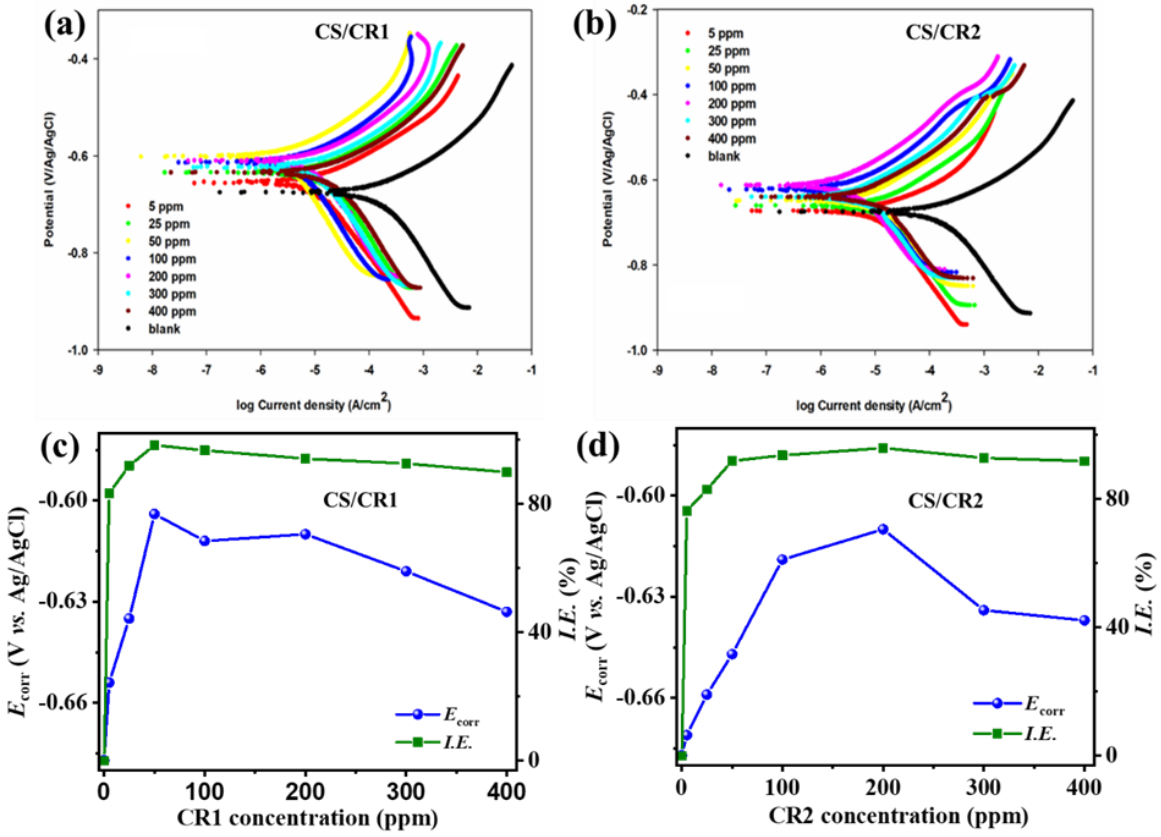

Fig. 4 (a, b) PDP curves and (c, d) Plots of E_{corr} and *I.E.* vs. inhibitors' concentrations of CS/CR1 and CS/CR2 in sweet/sour electrolyte (3.5 wt.% NaCl + 1000 ppm Na_2S + CO_2 purging) at 1000 rpm and 60 °C.

3.2.2 Partial SiO_2 deposit coverage with the inhibitors

The CS substrates that were partially and fully covered with SiO_2 deposit were used to test the corrosion prevention capabilities of CR1 and CR2. Measurements of PDP were carried out in sour conditions for immersion times (0 – 24 h). The initial E_{corr} for CS/SiO_2(partial)/CR1 (-715 mV) and CS/SiO_2(partial)/CR2 (-737 mV) showed higher negative corrosion potentials than for pristine CS (-677 mV) and inhibitor-treated CS without SiO_2 deposits (CS/CR1: -604 to -654 mV; CS/CR2: -610 to -671 mV) at all inhibitors concentrations (Fig. 5(a, b), Table S3). Given that the lower E_{corr} values imply lower energy barriers for iron oxidation, which are probably the result of the SiO_2 layer impeding inhibitor penetration, this suggests that partially SiO_2-covered samples are more susceptible to corrosion. However, E_{corr} values for CS/SiO_2(partial)/CR1 (-669 to -617 mV) and CS/SiO_2(partial)/CR2 (-713 to -638 mV) moved positively with prolonged immersion (6–24 h), reaching maximum at 12 and 24 h, respectively, indicating progressive inhibitor adsorption at the metal interface [69]. Lower anodic (b_a) and cathodic (b_c) Tafel slopes when compared to those without SiO_2 further supported the inhibitors' reduced protection in the presence of partial SiO_2 coverage. This was due to restricted diffusion and limited interfacial adsorption of inhibitors, which promoted the formation of iron oxidation and corrosion products. Notably, the E_{corr} departures from pristine CS, i.e., +60 mV for CS/CR1 and +39 mV for CS/CR2, remained below the 85 mV threshold value, indicating that CR1 and CR2 maintain their inhibition mechanism despite decreased efficacy by acting as mixed-type inhibitors even with partial SiO_2 coverage. Similar findings have been documented previously [69, 70]. The i_{corr} for partially covered samples with CS/CR1 (9.80–37.0 µA/cm²) and CS/CR2 (7.90–42.5 µA/cm²) were significantly lower than the pristine CS (147.0 µA/cm²) because of a negative shift in the anodic and cathodic polarization curves over time. This indicates that although partial SiO_2 deposition reduces the inhibitor's performance, it does not eliminate its protective effect.

The CS/SiO_2(partial)/CR1 and CS/SiO_2(partial)/CR2 had an elevated i_{corr} because of the partial deposition of SiO_2. The increase in i_{corr} was noteworthy because it was higher than those samples with both inhibitors without SiO_2 deposit, i.e., 2.60 µA/cm² for CS/CR1 and 6.20 µA/cm² for CS/CR2. However, the values for CS/SiO_2(partial)/CR1 and CS/SiO_2(partial)/CR2 were 9.8 µA/cm² at 12 and 7.9 µA/cm² at 24 h, respectively. The I.E. ranges show this trend, with CS/SiO_2(partial)/CR1 (74.8 – 93.3%) and CS/SiO_2(partial)/CR2 (71.1 – 94.6%), peaking at 12 h (93.3%) and 24 h (94.6%), respectively (Fig. 5(c, d)). These results show that the partial SiO_2 layer

hinders inhibitor performance since they are relatively lower than the efficiencies recorded for CS/CR1 (98.2%) and CS/CR2 (95.8%). The reduced diffusion of both CR1 and CR2 molecules through the incomplete SiO_2 deposit is the reason for this decrease in efficacy. The CR2 inhibitor's improved inhibitory efficacy over CR1 is due to its lower molecular size, which allows for better penetration and wider interfacial coverage inside the SiO_2 matrix at 24 h. The impact of SiO_2 partial coverage on inhibitor diffusion and performance further corroborated validated by the EIS data.

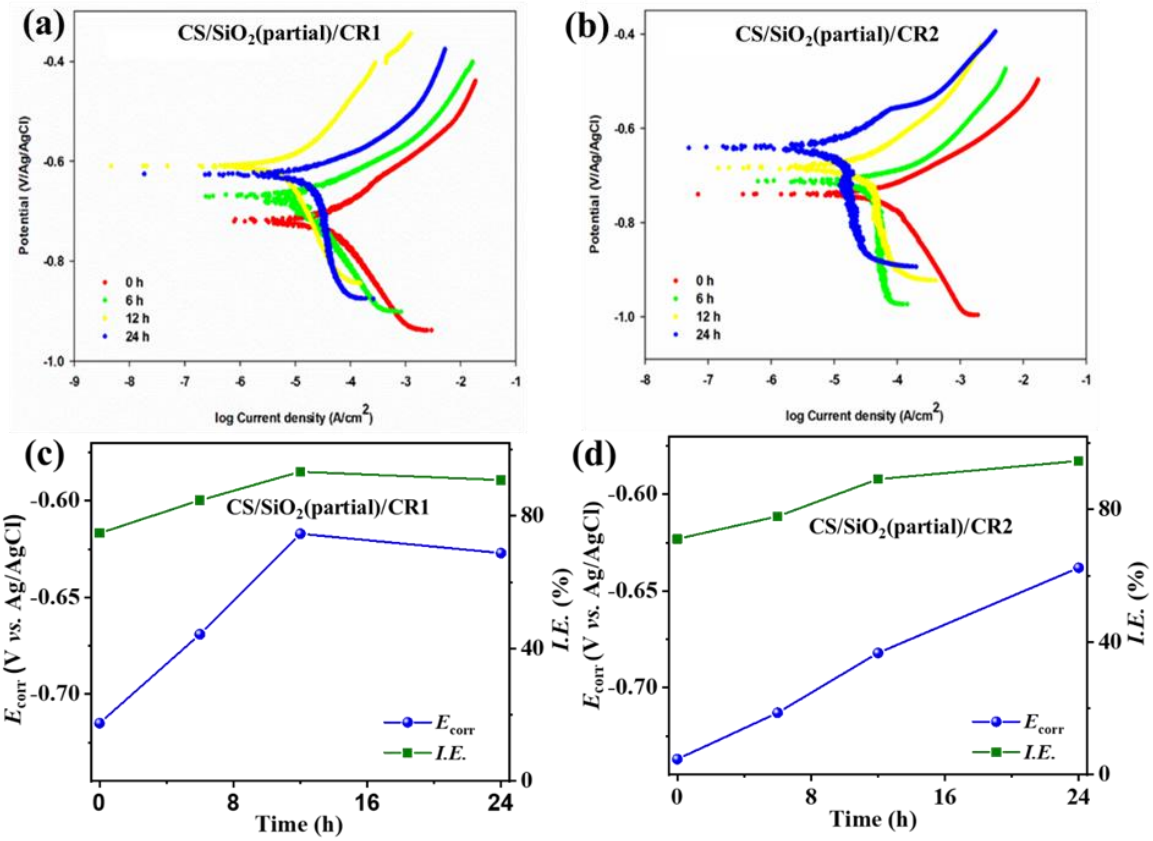

Fig. 5 (a, b) PDP curves and (c, d) Plots of E_{corr} and I.E. *vs* immersion time (0 – 24 h) of CS/SiO_2(partial)/CR1 and CS/SiO_2(partial)/CR2 in sour electrolyte (3.5 wt. % NaCl + 1000 ppm Na_2S + CO_2 purging) at 1000 rpm and 60 ºC.

3.2.3 Full SiO_2 deposit coverage with the inhibitors

When SiO_2 is fully deposited on CS, it creates an impenetrable physical barrier that blocks pore channels and prevents corrosion inhibitors from diffusing. Important insights into this phenomenon are provided by PDP analyses of CS/SiO_2(full)/CR1 and CS/SiO_2(full)/CR2 specimens carried out in simulated sour conditions (CO_2-saturated 3.5 wt% NaCl solutions

containing 1000 ppm Na_2S at 1000 rpm and 60°C) over immersion intervals (0 – 24 h) (Fig. 6(a, b)), with corresponding kinetic parameters compiled in Table S3. The fully developed SiO_2 layer at the first immersion (0 h) easily allows corrosive species like CO_2 and sulfide ions to enter, but it severely limits inhibitor penetration. Therefore, compared to pristine CS (-677 mV) and inhibitor-treated CS without SiO_2 (-604 mV for CS/CR1 and -610 mV for CS/CR2), E_{corr} for CS/SiO_2(full)/CR1 (-735 mV) and CS/SiO_2(full)/CR2 (-718 mV) are significantly more negative. These are also comparable to CS/SiO_2(partial)/CR1 (-715 mV) and CS/SiO_2(partial)/CR2 (-737 mV). This suggests that CS/SiO_2(full) is more vulnerable to corrosion in these circumstances, which can be attributed to the inhibitory blockage created by the complete SiO_2 coverage.

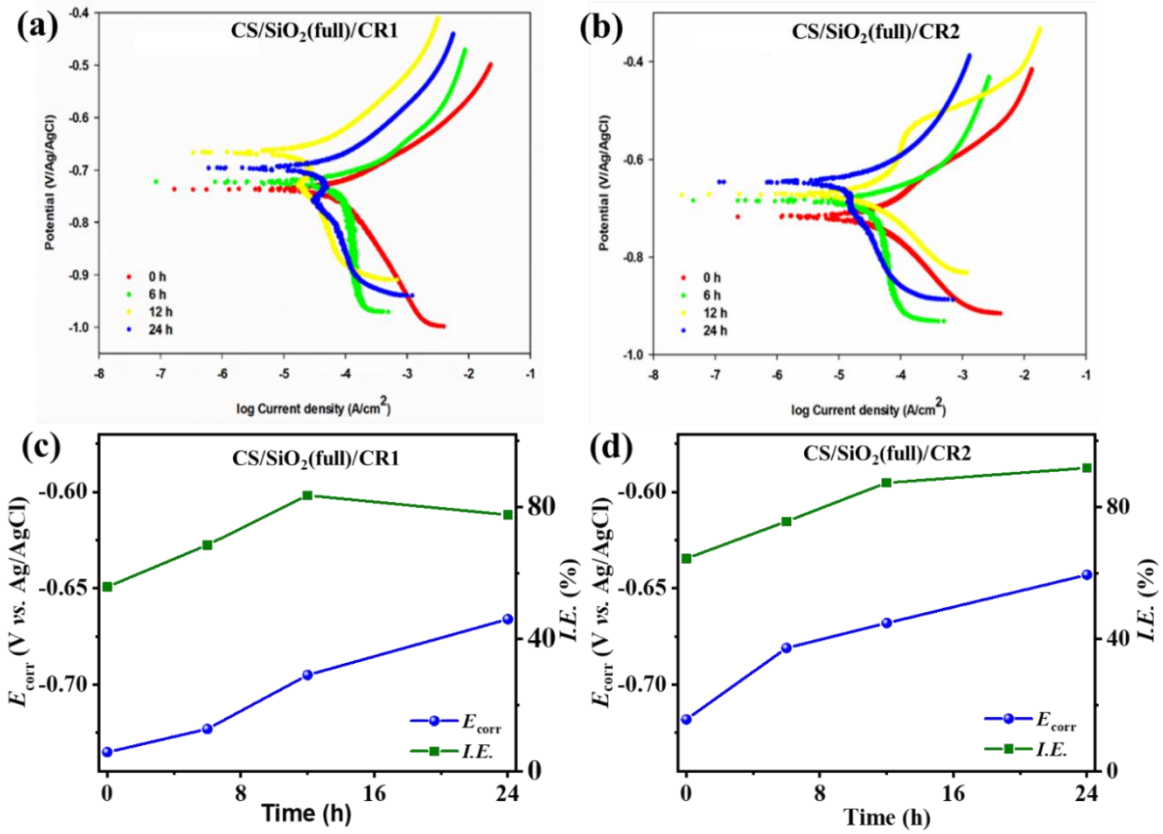

Fig. 6 (a, b) PDP curves and (c, d) Plots of Ecorr and IE vs immersion time (0 – 24 h) of CS/SiO_2(full)/CR1 and CS/SiO_2(full)/CR2 in sweet/sour electrolyte (3.5 wt. % NaCl + 1000 ppm Na_2S + CO_2 purging) at 1000 rpm and 60 ºC.

For CS/SiO_2(full)/CR1 (-723 to -666 mV) and CS/SiO_2(full)/CR2 (-681 to -643 mV) (Fig. 6(c,d)), a progressive positive shift in E_{corr} is shown during long immersion times (6–24 h),

indicating the slow diffusion and adsorption of CR1 and CR2 inhibitors through the SiO_2 layer. Despite this, the inhibitors' protective effectiveness is still lower than that of partially coated systems, as seen by higher anodic Tafel slopes (b_a) between 6 and 24 h that are similar to those of CS/SiO_2(partial)/CR1 and CS/SiO_2(partial)/CR2. This implies that interfacial adsorption is hampered by the limited inhibitor transport through the fully deposited SiO_2, which promotes localized corrosion and the development of corrosion products. When comparing pristine CS to CS/SiO_2(full)/CR1 (58 mV) and CS/SiO_2(full)/CR2 (41 mV), the observed deviation in E_{corr} values (less than 85 mV) shows that the inhibitors maintain a mixed-type inhibition mechanism regardless of SiO_2 coverage. The i_{corr} for CS/SiO_2(full)/CR1 (24.3 – 65.0 µA/cm²) and CS/SiO_2(full)/CR2 (12.0 – 52.5 µA/cm²) are increased due to the significantly compromised inhibitor performance caused by the fully deposited SiO_2 layer; minima are seen at 12 h (24.3 µA/cm²) and 24 h (12.0 µA/cm²), respectively. The results show that although the fully formed SiO_2 layer serves as a physical barrier, it paradoxically reduces the efficiency of inhibitors, making CS with complete SiO_2 coverage more susceptible to corrosion in sour environments.

Because the CR1 and CR2 inhibitors were less able to penetrate the SiO_2 layer, the i_{corr} values for fully deposited SiO_2 on CS were significantly higher than those for partially deposited SiO_2 on CS. Interestingly, over all immersion times, the i_{corr} values for the CS/SiO_2(full)/CR2 system were consistently lower than those for CS/SiO_2(full)/CR1, suggesting that CR2's smaller molecular size promotes better diffusion and interfacial adsorption on the CS surface, more successfully reducing corrosion. Furthermore, CS/SiO_2(full)/CR1 showed I.E. values (55.8 – 83.5%), peaking at 12 h, whereas CS/SiO_2(full)/CR2 showed I.E. values (64.4 – 91.8%), peaking at 24 h (Fig. 6(c, d)). These efficiencies are relatively lower than those observed for CS/CR1 (98.2%), CS/CR2 (95.8%), CS/SiO_2(partial)/CR1 (93.3%), and CS/SiO_2(partial)/CR2 (94.6%), underlining that the complete SiO_2 deposition impedes inhibitor effectiveness due to reduced inhibitor diffusion. Nevertheless, the lower steric bulk of CR2 facilitates improved diffusion relative to CR1 after prolonged immersion, resulting in higher inhibition performance for CS/SiO_2(full)/CR2. The impact of inhibitor molecular size and SiO_2 deposition thickness on corrosion protection effectiveness further supported by the EIS results.

Overall, using various electrochemical evaluation techniques, the CR1 and CR2 inhibitors showed significant differences in I.E. when applied to CS surfaces that were partially and completely covered with SiO_2 compared to uncovered CS. When CR1 and CR2 were present, the

I.E. values for CS with partial SiO_2 coverage dropped by 3.1% and 0.7%, respectively, according to EIS analysis. Conversely, CS samples that were fully SiO_2 covered showed a more noticeable decrease in I.E., with drops of 2.7% for CR2 and 5.9% for CR1. These patterns were further emphasized by the PDP measurements, which revealed a more pronounced reduction in inhibition performance: the I.E. of CS/SiO_2(partial) dropped by 4.9% and 1.2% with CR1 and CR2, whereas the CS/SiO_2(full) samples showed reductions of 14.7% and 4.0% with CR1 and CR2, respectively. All of these findings show that the efficiency of both commercial inhibitors is significantly reduced on the fully covered SiO_2 layer on the CS surface, with the effect being more noticeable when PDP analysis is used. This implies that the adsorption and protective function of CR1 and CR2 on the metal surface are impeded by the barrier-like effect of the SiO_2 layer.

3.3 Physical characterization

Surface characterization techniques, including SEM, EDX, XRD, XPS, and contact angle measurements, were systematically employed to comprehensively evaluate the physicochemical properties of inhibited CS coupons. The analyses focused on key parameters such as surface morphology, elemental compositions, crystallographic structure, chemical states, and wettability characteristics, comparing samples with and without silicon dioxide (SiO_2) deposits exhibiting both partial and full coverage. Subsequently, the impact of corrosive species beneath the SiO_2 deposits on the inhibited CS surfaces was investigated by assessing changes in the physicochemical merits after 24 h of immersion in sour electrolyte. This approach enabled a detailed understanding of the interplay between SiO_2 coverage and corrosion inhibition efficacy under simulated corrosive conditions.

3.3.1 Scanning electron microscope and energy-dispersive X-ray spectroscopy

After 24 h of electrochemical corrosion testing in sour electrolyte, the SEM micrographs show the surface morphology of CS/CR1, CS/CR2, CS/SiO_2/CR1, and CS/SiO2/CR2 (Fig. 7). The CS/CR1 and CS/CR2 showed compact, dense coatings that were free of noticeable breaking. Due to the comparatively bulky CR1 inhibitor's adsorption on the CS surface, the CS/CR1 samples specifically showed aggregated, spongy-like structures that, at greater magnification, revealed fine rod-like topologies without discernible pores (Fig. 7(a), inset). However, at both low and high magnifications, the CS/CR2 samples showed a morphology with small, flake-like characteristics

and some visible pores (Fig. 7(b), inset). This morphological difference illustrates how the two inhibitors behaved differently in terms of adsorption and film development during the corrosion tests.

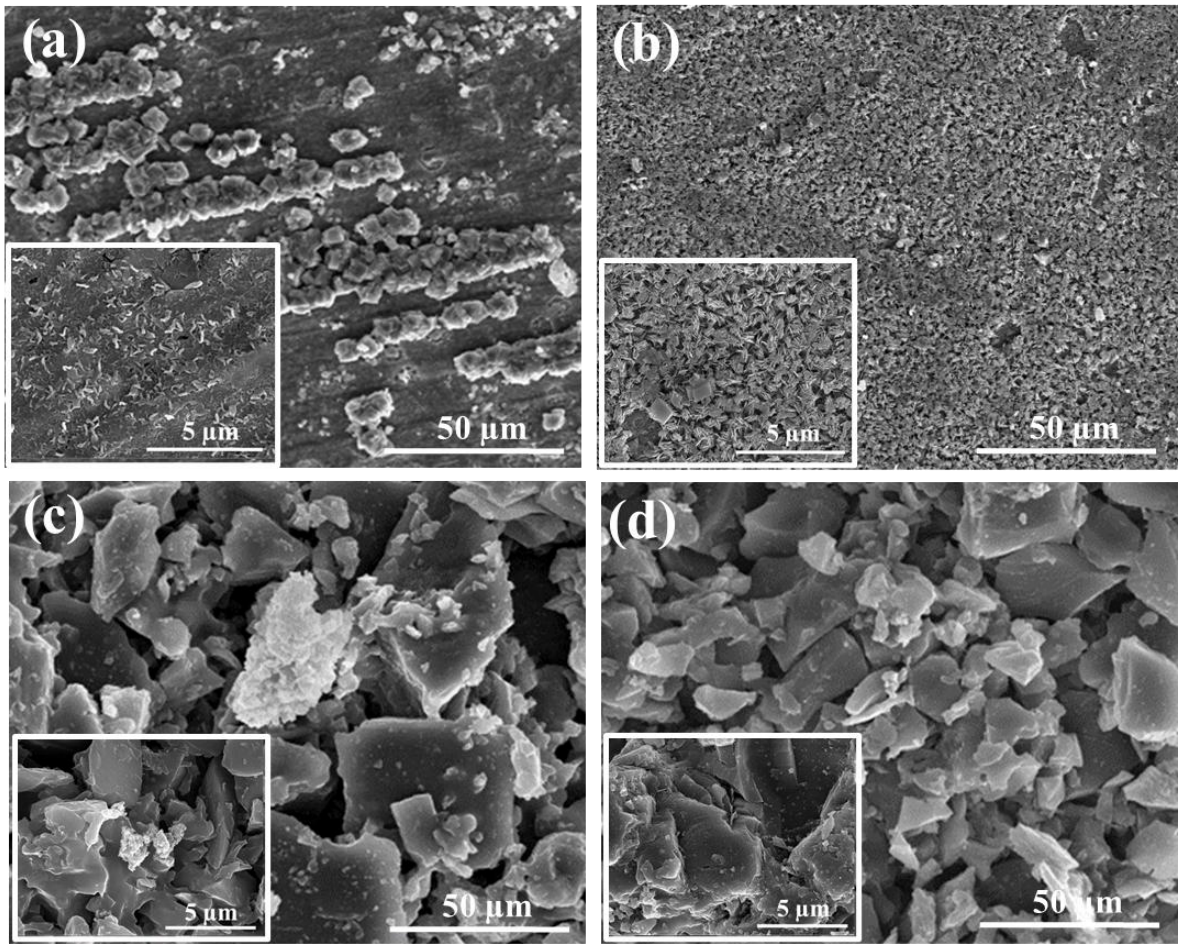

Fig. 7 SEM micrographs with inset high magnification of (a) CS/CR1, (b) CS/CR2, (c) CS/SiO_2/CR1 and (d) CS/SiO_2/CR2 after electrochemical corrosion tests for 24 h in the sweet/sourtest electrolyte.

Although the CS surface is uniformly covered with CR2, the SiO_2 deposit's porosity prevents CR2 molecules from diffusing directly to the underlying CS substrate, reducing the system's ability to suppress corrosion in comparison to the CS/CR1. According to corrosion testing in a simulated sour electrolyte, the bulkier CR1 molecules show more effective interfacial adsorption on the CS surface than the less bulky CR2, as indicated by the compactness and shape of the inhibitor films. Significantly, the CS/SiO_2/CR1 and CS/SiO_2/CR2 samples showed

agglomerated, irregular flaky structures, indicating that the presence of the SiO_2 layer on the inhibited CS surface significantly changed the surface morphology (Fig. 7c,d). These structural changes are ascribed to iron oxide crystallite phases that were created as a result of accelerated iron dissolution beneath the SiO_2 layer, phenomena that were not present in the non-SiO_2-coated samples and are noticeably larger than those on samples without SiO_2 deposition (CS/CR1 and CS/CR2). The inhibitors' ability to provide protection is hampered by the corroded features underneath the SiO_2 deposit. The observed decrease in I.E of CR1 and CR2 on SiO_2-covered CS surfaces is probably caused by the inhibitor molecules' preferential adsorption onto the SiO_2 surface as opposed to the CS substrate, as well as the simulated sour electrolyte's easy passage through the porous SiO_2 layer [30, 71]. However, in comparison to CR1, CR2 exhibits better compatibility with the SiO_2 deposit, allowing for more efficient penetration through the deposit pores, especially after 24 h of immersion. This results in improved corrosion inhibition effectiveness. This phenomenon offers a mechanical explanation for why CR2 has better UDC resistance than CR1.

EDX analysis was used to probe the surface compositions of inhibited CS coupons, both with and without SiO_2 deposits, both qualitatively and quantitatively. Nitrogen (N), oxygen (O), carbon (C), phosphorus (P), iron (Fe), sulfur (S), sodium (Na), and oxygen (O) were found to be present in amounts of 25.4/22.5/15.2/14.5/12.7/5.8/3.9 wt.% for CS/CR1 and 23.2/23.2/15.9/12.6/14.5/5.7/4.9 wt.% for CS/CR2 (Fig. S2(a, b), Table S4). These findings suggest a more considerable and consistent inhibitor film generation that successfully lowers Fe exposure on the CS surface, as well as a larger concentration of heteroatoms (O, N, and P) on the CR1-treated surface. As a result, in sour electrolyte situations, CR1 performs better than CR2 at inhibiting corrosion. However, the high concentrations of Na, C, and Fe found on the CS/CR2 surface suggest that electrolyte penetrated through the steel substrate's porous areas, promoting localized dissolution and the production of corrosion products, which reduces the effectiveness of the inhibition [72, 73]. The elemental profiles after SiO_2 deposition on CS with the inhibitors agree with earlier findings. The presence of C/O/Na/S/N/P/Fe/Si was determined by EDX analysis of SiO_2-covered samples treated with inhibitors at 18.90/23.10/14.50/2.07/8.37/3.36/18.80/2.07 wt.% for CR/SiO_2/CR1 and 17.20/24.50/11.40/2.00/12.30/5.30/16.70/10.6 wt.% for CR/SiO_2/CR2 (Fig. S2(c, d), Table S4). In comparison to CR/SiO_2/CR1, CS/CR1, and CS/CR2 samples, the substantially higher concentrations of Si, N, P, and O on the CR/SiO_2/CR2 surface imply that the

CR2 inhibitor penetrates and interacts with the SiO_2 layer rather than the underlying CS substrate more effectively, leading to a weaker protective film formation and reduced corrosion resistance. The adsorption of both CR1 and CR2 inhibitors onto the CS surfaces, with and without SiO_2 deposits, albeit to differing degrees, was further validated by SEM in conjunction with EDX. The efficiency of the inhibitor films in reducing corrosive deterioration is highlighted by the significant correlation between the absence of surface fractures on inhibited CS specimens and the low CRs observed during electrochemical testing.

3.3.2 Contact angle measurements

The contact angle (θ_C) is a crucial metric for evaluating surface wettability, which is the angle created at the interface between a liquid droplet and a solid surface. Surfaces exhibiting a θ_C (<90°) are hydrophilic, those with θ_C (> 90° but <150º) are deemed hydrophobic and surfaces with θ_C (> 150°) are superhydrophobic [74]. In this investigation, samples were subjected to electrochemical corrosion testing in the electrolyte at 60°C with 1000 rpm agitation for 24 hours before contact angle measurements were made. The inhibited carbon steel (CS) samples, referred to as CS/CR1 and CS/CR2, showed contact angles of 135° and 129°, respectively (Fig. 8(a, b)), suggesting that both samples were significantly hydrophobic, with CS/CR1 exhibiting the better hydrophobic properties. Increased hydrophobicity is associated with decreased surface wettability, which reduces the tendency of water molecules and corrosive ions to adhere to the metal surface. This decrease in surface wetting is a major factor in the samples' improved corrosion inhibition performance [75]. SiO_2 deposition on CS with corrosion inhibitors (CR1 and CR2) significantly reduces the surface hydrophobicity, i.e., θ_C reductions of 36.8% and 25.5% for CS/SiO_2/CR1 (85.6°) and CS/SiO_2/CR2 (96.2°), respectively, and the CS/SiO_2/CR1 becomes hydrophilic while CR2 remains hydrophobic (Fig. 8(c, d)). This differential behavior supports the superior corrosion inhibition performance of CR2 on SiO_2-covered CS over long immersion times, while CS/SiO_2/CR1 samples exhibit increased surface wettability, which promotes corrosive degradation of the CS/SiO_2/CR1 interface. These results agree with the electrochemical corrosion data and support the link between surface wettability modifications and inhibitor efficacy under SiO_2 deposition.

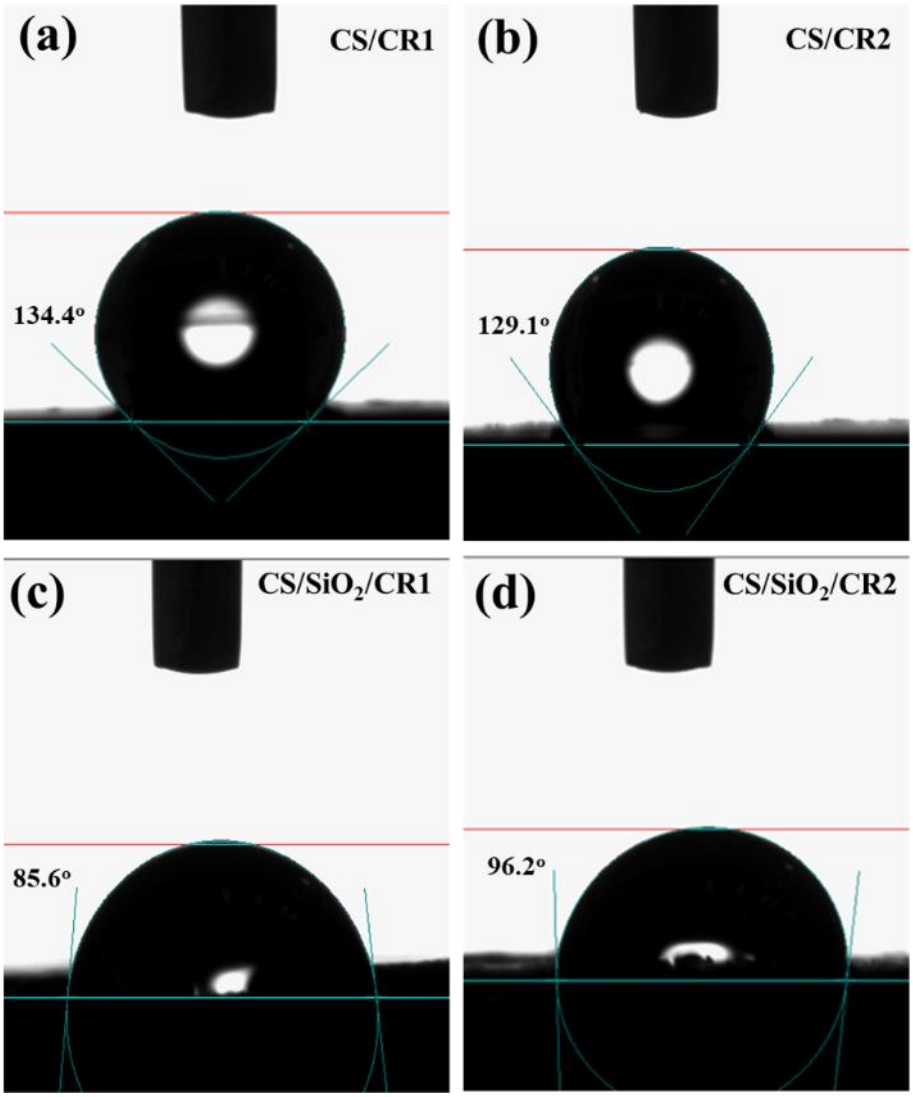

Fig. 8 Contact angle measurements of (a) CS/CR1, (b) CS/CR2, (c) CS/SiO_2/CR1 and (d) CS/SiO_2/CR2 after electrochemical corrosion tests for 24 h in the electrolyte.

3.3.3 X-ray diffraction

XRD was used to analyze the crystallographic structure of CS samples, with/without CR1 and CR2 inhibitors, and presence/absence of SiO_2 deposition after 24 h immersion in a sour electrolyte. Using ICDD code 98-018-6832, the XRD patterns of pristine CS, CS/CR1 and CS/CR2 revealed Fe facets {110}, {200}, and {211}, which corresponded to cubic structures with Im-3m symmetry (Fig. 9(a)). Interestingly, the CS displayed a broad {011} peak attributed to amorphous FeS, indicating the formation of a passive mackinawite sulfide layer on the surface under sour

conditions [76]. This peak was absent in the CS/CR1 and CS/CR2 samples, demonstrating that CR1 and CR2 successfully reduced passive sulfide production. Additionally, the Fe{110} peak in CS/CR1 and CS/CR2 shifted to higher Bragg angles (44.75° and 44.77°, respectively) with greater full width at half maximum (FWHM) values (0.2338 and 0.2412) compared to pristine CS (44.66°; 0.2152) (Fig. 9(b)). The adsorption of CR1 and CR2 inhibitors at the CS surface is responsible for this shift and peak broadening, which show lattice contraction, decreased crystallite size, and higher lattice strain in the Fe matrix [77], which impedes Fe dissolution and subsequent corrosion product formation.

In addition to Fe diffraction peaks (Fig. 9(c)), XRD analysis of the SiO_2-covered samples (CS/SiO_2, CS/SiO_2/CR1, and CS/SiO_2/CR2) showed several SiO_2 facets ({010}, {110}, {011}, {201}, {111}, {020}, {211}, {301}, {121}, {302}, {203}, and {122}) with hexagonal symmetry (P3121). Effective surface covering by the SiO_2 layer is proven by the SiO_2 diffraction signals' dominance over Fe. This covering, however, might make it easier for the sour electrolyte to penetrate while impeding the quick diffusion of inhibitors, which could exacerbate corrosive deterioration in sour environments. The structural changes brought about by inhibitors and SiO_2 coverage that affect corrosion resistance mechanisms in CS exposed to sour conditions are clarified by the XRD investigation [71]. Shifts in the SiO_2 {110} diffraction peak, observed at lower and higher Bragg angles for the CS/SiO_2/CR1 (26.58°) and CS/SiO_2/CR2 (26.79°) samples, respectively, relative to the pristine CS/SiO_2 system (26.71°) (Fig. 9(d)), indicate distinct modes of inhibitor adsorption at the SiO_2 interface. The preferential adsorption of CR1 and CR2 inhibitors, characterized by their abundant electron-withdrawing and electron-donating functional groups, takes place through the SiO_2 layer on the carbon steel (CS) surface. It is noteworthy that the FWHM values for CS/SiO_2, CS/SiO_2/CR1, and CS/SiO_2/CR2 do not change, indicating that the inhibitors have no effect on the size of the crystallites. This implies that the inhibitors do not cause the SiO_2 lattice to undergo any notable structural changes. Therefore, compared to inhibitor-treated samples without the SiO_2 deposit (CS/CR1 and CS/CR2), the corrosion inhibition efficacy is reduced due to the lack of significant synergistic effects and restricted direct interaction between the inhibitors and the CS substrate.

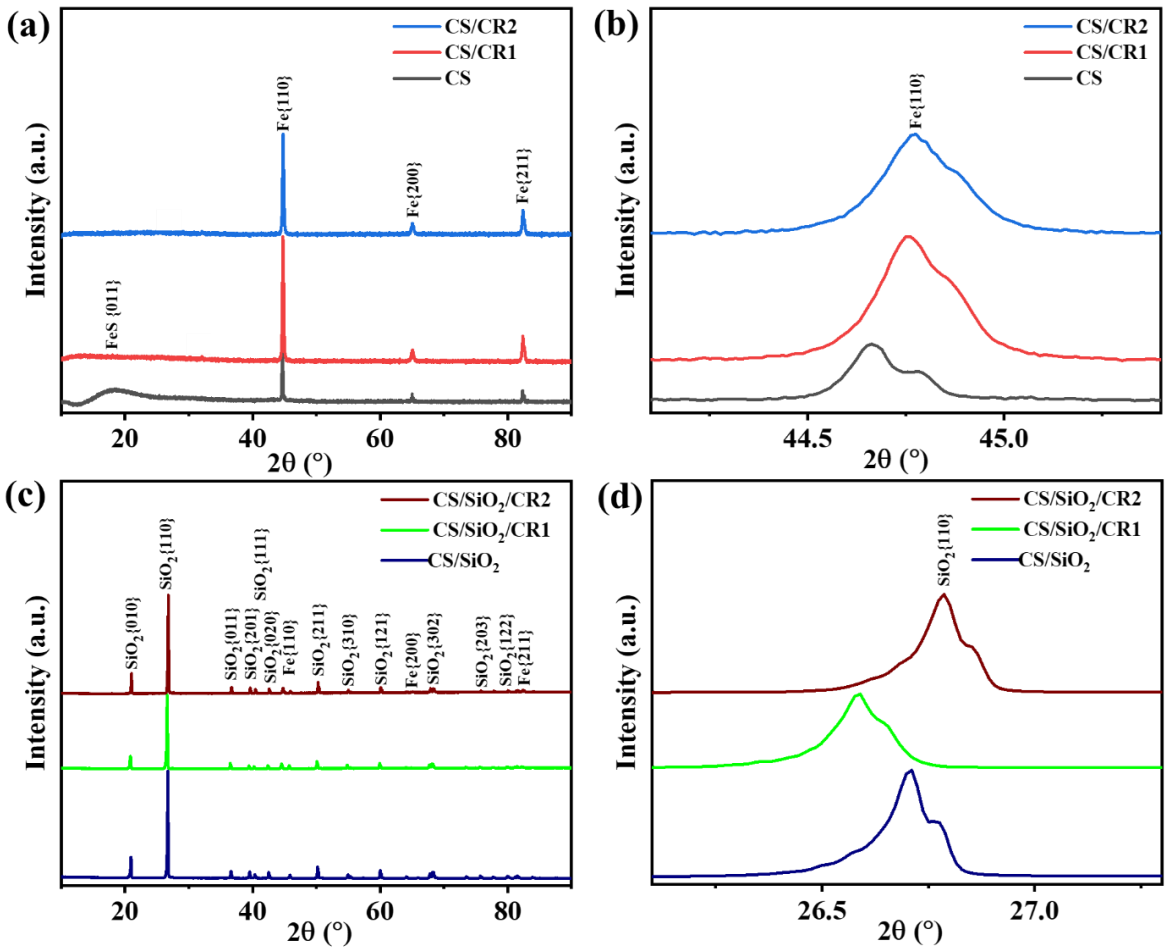

Fig. 9 XRD spectra of (a) CS, CS/CR1 and CS/CR2, (b) enlarged {110} facet of Fe, (c) CS/SiO_2, CS/SiO2/CR1 and CS/SiO_2/CR2 and (d) enlarged {110} facet of SiO_2 after electrochemical corrosion tests for 24 h in the simulated sour electrolyte.

3.3.4 X-ray photoelectron spectroscopy

The interfacial chemical states of CS exposed to sour electrolyte with CR1 and CR2 were examined using XPS following a 24 h immersion, both with and without SiO_2 deposits. Uninhibited surfaces had strong Fe 2p, C 1s, O 1s, S 2p, and N 1s core-level transitions, along with valence-level Fe 3s and Auger FeLMM-2 features, according to wide-scan XPS spectra (Fig. S3(a)), which demonstrated unique elemental compositions. Increased Fe 2p, S 2p, and FeLMM-2 signals for inhibited CS without SiO_2 (CS/CR1, CS/CR2) suggested robust inhibitor adsorption on the metallic substrate, which is in line with the formation of protective films. The SiO_2-deposited samples (CS/SiO_2/CR1, CS/SiO_2/CR2), on the other hand, showed suppressed Fe-related

spectral intensities and enhanced Si 2p/Si 2s signals, indicating preferential inhibitor adsorption onto the SiO_2 layer instead of direct steel interaction. This interfacial decoupling creates a permeable barrier that permits electrolyte ion penetration while blocking inhibitor-steel contact, which increases UDC susceptibility through localized electrochemical activity. High-resolution core-level spectra further clarified chemical bonding environments, confirming the crucial role of deposit-mediated adsorption mechanisms in controlling corrosion dynamics.

Deconvoluting the high-resolution Fe 2p spectra into the distinctive doublet peaks that correspond to Fe $2p_{3/2}$ and Fe $2p_{1/2}$ revealed that the CS sample was primarily composed of Fe^{2+}:708.0 and 721.6 eV; Fe^{3+}:710.6 and 724.8 eV; and Fe^{2+} shake-up satellite: 715.6 and 729.4 eV (Fig. 10(a)). Meanwhile, the deposition of SiO_2 shifted these spectra to slightly higher binding energies in CS/SiO_2 sample, i.e., Fe^{2+}: 708.2 and 721.7 eV; Fe^{3+}: 710.8 and 724.8 eV; and Fe^{2+} shake-up satellite: 715.7 and 729.6 eV. Although the binding energy of Fe^{2+} $2p_{3/2}$ is always found around 709 eV, but experimentally possible shift to around 708 eV could be observed, due to specific chemical species, like surface effects, intermolecular interactions, lattice environment, ligand field, and crystal structure [78-80]. This finding implies more oxidized Fe species are formed with SiO_2 deposition. When corrosion inhibitors CR1 and CR2 were added without SiO_2 deposition, the Fe d-band center was slightly shifted, as evidenced by slightly lower binding energies in CS/CR1 (Fe^0: 707.0 and 719.9 eV; Fe^{2+}: 709.2 and 722.4 eV; Fe^{3+}: 711.3 and 723.9 eV; Fe^{2+} shake-up satellite: 715.2 and 729.8 eV) and CS/CR2 (Fe^0: 706.5 and 719.4 eV; Fe^{2+}: 708.2 and 720.7 eV; Fe^{3+}: 710.8 and 723.4 eV; Fe^{2+} shake-up satellite: 715.1 and 729.7 eV). This change implies that both inhibitors successfully prevent iron oxides from forming higher oxidation states. Conversely, an upshift in the Fe d-band center to higher binding energies in CS/SiO_2/CR1 (Fe^{2+}: 707.9 and 721.5 eV; Fe^{3+}: 710.6 and 725.5 eV; Fe^{2+} shake-up satellite: 715.5 and 729.9 eV) and CS/SiO_2/CR2 (Fe^{2+}: 708.0 and 721.2 eV; Fe^{3+}: 710.5 and 724.4 eV; Fe^{2+} shake-up satellite: 715.9 and 730.9 eV) demonstrate that the presence of a SiO_2 layer promoted an increase in Fe oxide formation. Interestingly, CR2's lower molecular size allows it to more efficiently penetrate the SiO_2 deposit, which mitigates the development of Fe oxide to a greater degree than the larger CR1 molecule, which shows less penetration through the SiO_2 layer [55, 56].

Four different chemical states were identified by deconvolution of the C 1s spectra for pristine CS, CS/CR1, and CS/CR2 samples. These states corresponded to C=C/C–C, C–O, C=O, and O–C=O at binding energies of 284.7, 285.8, 287.0, and 288.4 eV, respectively, with dominant

peak of C=C/C–C (Fig. 10(b)). The O–C=O signal was not present in the CS/SiO_2, CS/SiO_2/CR1, or CS/SiO_2/CR2 samples after SiO_2 was added. Significant absorption characteristics related to carbides, notably Fe–C at 283 eV and Si–C at 282 eV, were made possible by the addition of CR1 and CR2 inhibitors. Also, these inhibitors caused a significant decrease in oxide species, which is why the CS/SiO_2 sample had peaks for Fe–C, C=C/C–C, C–O, and C=O, while the CS/SiO_2/CR1 sample had signals for Si–C, Fe–C, C=C/C–C, C–O, and C=O, and the CS/SiO_2/CR2 sample had Si–C, Fe–C, C=C/C–C, and C–O peaks. These findings imply that the CR2 inhibitor suppresses carbon oxidation more efficiently when SiO_2 deposits are present, demonstrating its superior antioxidative capacity in these circumstances.

The high-resolution O 1s area identified three different components that corresponded to Fe–O bonds, oxygen vacancies, and surface hydroxyl groups ($^{-}$OH) in all samples that were examined, including CS, CS/SiO_2, CS/CR1, CS/CR2, CS/SiO_2/CR1, and CS/SiO_2/CR2 (Fig. 10(c)). These characteristics show that H_2O and O_2 species are firmly adsorbed on the sample surfaces. The chelation of Fe atoms with the oxygen-containing terminal groups of the corrosion inhibitors is responsible for the notable production of passive iron oxides on CS/CR1, CS/CR2, CS/SiO_2/CR1, and CS/SiO_2/CR2 samples in the sour environment. In contrast, this passivation was less noticeable in the CS and CS/SiO_2 samples, highlighting the impact of inhibitor–surface interactions on oxide formation in corrosive environments.

The simulated sour atmosphere that was created for H_2S during the corrosion experiments is what caused the S 2p signal to be detected. Characteristic spin-orbit coupling peaks were identified by multiple S species of the S 2p spectra for CS and CS/SiO_2 samples (Fig. S3(b)). The different sulfur species include elemental sulfur ($2p_{3/2}$ and $2p_{1/2}$ of S^0), sulfides ($2p_{3/2}$ and $2p_{1/2}$ of SO_3^{2-}), sulfites ($2p_{3/2}$ and $2p_{1/2}$ of SO_3^{2-}), and sulfates ($2p_{3/2}$ and $2p_{1/2}$ of SO_4^{2-}). These findings show that sulfide, sulfite, and sulfate ions readily penetrate and adsorb onto both CS and CS/SiO_2 surfaces in the absence of CR1 and CR2 corrosion inhibitors. On the other hand, as indicated by the spin-orbit coupling peaks for S_2^{2-} ($2p_{3/2}$ and $2p_{1/2}$) (Fig. S3(c)), the addition of CR1 and CR2 significantly reduced the creation of sulfite and sulfate species on CS/CR1, CS/CR2, CS/SiO_2/CR1, and CS/SiO_2/CR2 samples, while enabling only the presence of disulfide species. The CR1 and CR2 inhibitors work by adsorbing sulfide species from the sour electrolyte to successfully mitigate corrosive assault. However, SiO_2 deposit prevents the species from interacting directly with the CS substrate.

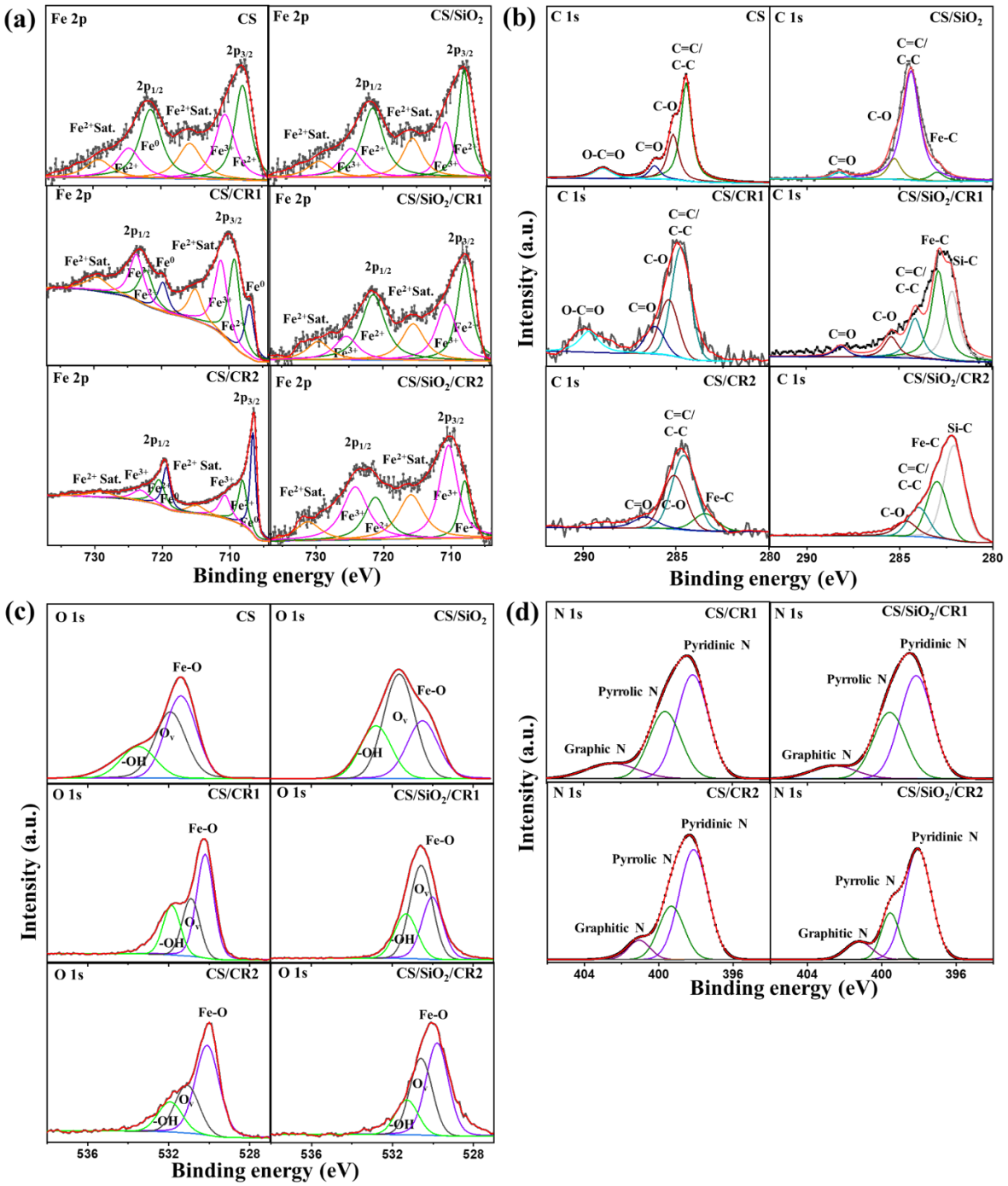

Fig. 10 Deconvoluted spectra of (a) Fe 2p, (b) C 1s, (c) O 1s, and (d) N 1s of CS, CS/SiO_2, CS/CR1, CS/CR2, CS/SiO_2/CR1, and CS/SiO_2/CR2 after electrochemical corrosion tests for 24 h in the sour electrolyte.

Three separate components representing pyridinic N, pyrrolic N, and graphitic N species were identified from the deconvoluted N 1s spectra of the inhibitor-containing samples (Fig. 10(d)), in both the presence and absence of SiO_2. These findings show that the inhibitors' amine functional groups help to create and stabilize nitrogen-containing linkages on the CS surface. The CS substrate's resistance to corrosion is increased by these nitrogen functionalities, which facilitate efficient coordination interactions that prevent the formation and spread of corrosion products.

3.4 Interfacial mechanism of the commercial inhibitors for under-deposited corrosion of carbon steel

Along with physicochemical characterizations (SEM, EDX, contact angle measurements, XRD, and XPS, the electrochemical analyse (EIS and PDP), collectively show the superior corrosion inhibition performance of commercial inhibitors toward UDC on CS coupons with partially and fully covered SiO_2 deposits. CR2 inhibitor compounds' superior interfacial adsorption and penetration through SiO_2 deposit relative to CR1 inhibitor are the main causes of this increased inhibition. Interfacial interactions involving electron transfer through conjugated π-bonds and/or heteroatoms between the inhibitor molecules and Fe atoms on the steel surface enable both CR1 and CR2 to molecularly adsorb onto the Fe atoms of the CS substrate, which is intrinsically linked to their corrosion inhibition efficacy [81, 82]. Such adsorption substantiates their inherent anticorrosive capabilities by successfully blocking the diffusion and adsorption of aggressive corrosive species, such as carbonates (CO_3^{2-}), sulfides (S^{2-}), hydrogen (H^+), and chloride (Cl^-) ions.

However, the effectiveness of these inhibitors in inhibiting corrosion is significantly reduced due to their relatively high molecular lengths, which limit their ability to penetrate the SiO_2 layer coverage on CS. Strong electrostatic adsorption of the inhibitors onto the SiO_2 rather than the underlying CS substrate is promoted by the sour electrolyte's acidic pH, which gives the SiO_2 surface a negative charge [70]. Because of this preferential binding, less inhibitors are available at the steel interface, which makes it easier for sour electrolytes to reach the CS surface and spread UDC even in the presence of inhibitors. The inhibitors' capacity to permeate through SiO_2 pores and adsorb at the CS interface in the simulated sour circumstances under investigation is controlled by their molecular size and hydrophobicity, which are further exacerbated by the SiO_2 deposit's partial/full surface coverage of CS. This mechanistic realization, illustrated in Scheme 2,

clarifies that CR2 has a higher inhibitory efficacy in the presence of SiO_2 deposits than the bulkier CR1 inhibitor due to its decreased steric bulk and increased hydrophobicity.

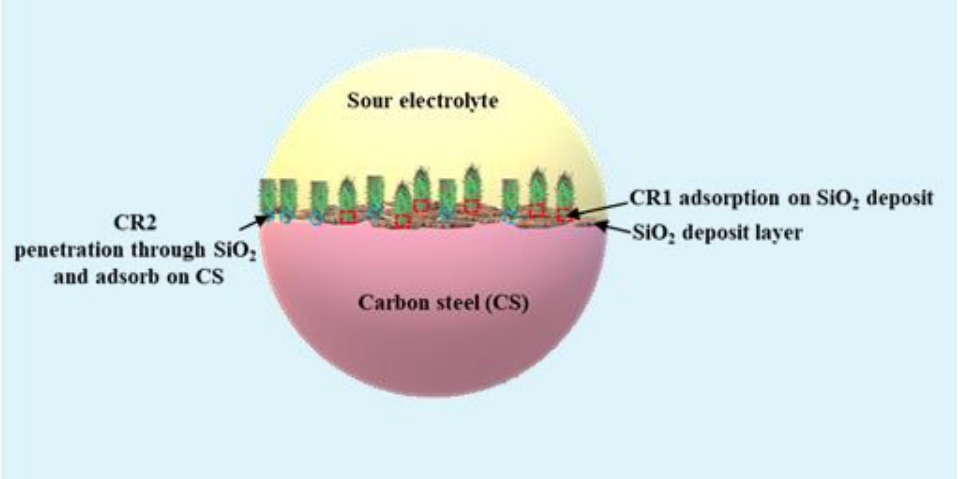

Scheme 2 Interfacial Mechanism of the CR1 and CR2 inhibitors for SiO_2 under-deposited corrosion of CS.

3.5. Applicability of machine learning models

This study focuses on the utilization of various ML models for the prediction of localized corrosion of CS, particularly inhibition efficiencies of CR1 and CR2 inhibitors toward SiO_2 under-deposited corrosion of CS, from the datasets obtained from two electrochemical methods (Tables 1, S1 – S3). This approach uniquely combines data from both EIS and PDP methods to create sufficient datasets for models' development and enhance the models' robustness and predictive capabilities. Unlike previous research efforts that extract datasets from a single electrochemical method or weight loss measurements [33, 34, 36], Hence, data points were categorized as (a) electrochemical methods (EIS or PDP); (b) SiO_2 deposit (partial or full coverage); and (c) corrosion inhibitor (CR1 or CR2) is converted into one-hot vectors for use by the ML models, as shown by the correlation matrix of the entire dataset (Fig. 11(a)). The total number of data points is 60, of which 30 are from PDP and 30 are from EIS. Then, the data points are segregated into inhibitor efficiency (*I.E.*) as output and all other variables as input for model development. The total dataset is split into training (80%) and testing (20%) datasets, maintaining the same ratio for each electrochemical method. Since all the data-points are numerical, various ML regression models were applied including: (i) linear regression (LR), (ii) k-nearest neighbor (KNN) regressor, (iii) random forest

(RF) regressor, (iv) decision-tree (DT) regressor, (v) gradient-boosting (GB) regressor, and (vi) extreme gradient-boosting (XG) regressor [83].

Feature importance studies were methodically carried out using an integrated framework of complimentary approaches in order to create a solid, multivariate understanding of predictor variable contributions (Table S5): (i) By calculating SHAP (SHapley Additive exPlanations) values for both the RF and XGB algorithms, model-agnostic interpretability was attained, offering interpretable measures of global and local feature impacts across nonlinear decision boundaries; (ii) Intrinsic impurity-based importance metrics from RF and permutation importance scores from XGB were simultaneously analyzed to empirically validate the dominant influence of SiO_2 deposit morphology and temporal exposure parameters; and (iii) Using directional visualization and coefficient magnitude analysis, linear regression coefficients were quantitatively evaluated to allow for a direct comparison of effect sizes under linear assumptions (Table S6).

SiO_2 deposit and exposure length (partial or full) were revealed to be the main factors influencing UDC behavior across all models that were tested by multivariate analysis. To maintain generalizability under diverse experimental configurations, the concentration of inhibitors parameter was kept in the final model architecture even though it lacked statistical significance ($\alpha = 0.05$) in linear regression models. The analysis used five complementary approaches to fully quantify feature contributions: (i) Linear Regression Coefficients and their statistical significance (Fig. S4a); (ii) Random Forest Feature Importance (Fig. S4b); (iii) XGBoost Feature Importance (Fig. S4c); (iv) SHAP Feature Importance for Random Forest (Fig. S4d); and (v) SHAP Feature Importance for XGBoost (Fig. S4e). The potential biases associated with individual interpretation methodologies were addressed using the multimodal approach, which guaranteed robust characterization of parameter influence through both model-specific metrics (coefficients, gain scores) and model-agnostic game-theoretic valuation (SHAP).

The models' performance metrics were evaluated with respect to R^2, RMSE and MAE for the training and testing results, summarized in Table 2. Fig. 11(b-d) clearly denotes the whole dataset's actual and predictions, which are the primary focus for model evaluation. The training results reveal that RF, XGB, DT and GB have promising performance metrics for this study, but LR and KNN models were inappropriate. However, the RF and XGB regressors were first explored to reveal the actual and predicted I.E. of CR1 and CR2 toward SiO_2 (partial or full coverage) deposited CS in simulated sour conditions (Fig. 11(b)). The initial testing results delivered R^2,

RMSE and MAE of 0.90, 3.6% and 2.7%, respectively for RF regressor, which are superior to XGB (0.85; 4.6% and 3.0%). Then, we reconstructed the training-testing dataset with 80-20 split for four-folds cross validation (CV) to evaluate the repeatability of the viable regressions (RF, XGB, DT and GB) and prevent overfitting [84]. The RF ($R^2 = 0.85 \pm 0.05$) and XGB ($R^2 = 0.84 \pm 0.03$) are capable of consistently providing mean $R^2 > 0.80$ for all the four iterations from dataset extracted from EIS and PDP (Fig. 11(c, d)).

However, the RF regressor is the best predictive ML model with a high R^2, but the least RMSE and MAE compared to XGB, GB, DT, KNN, and LR (Figure 11e, f). The RF regressor had previously been employed as the best algorithm for corrosion rates-time series prediction of CS in sweet conditions [43]. A prior approach models the corrosion inhibition using inhibition power (P_{inh}) expressed in equation 6 [85]. In a similar vein, this study attempted to model P_{inh} as the output and the model yielded a similar output to the presented output (Table S6). The transformation to P_{inh} led to a more symmetric and Gaussian-distributed target, resulting in improved model robustness and predictive performance, particularly for ensemble-based models such as XGBoost and Random Forest. This work is the first to report that random forest (RF) regressor is the most appropriate ML model for studying the UDC corrosion of CS in simulated sour conditions utilizing commercial inhibitors.

Table 2 Summary of performance metrics using various ML algorithms

ML Models	Training results			Testing results			4-fold CV R^2 (mean ± std)
	R^2	RMSE (%)	MAE (%)	R^2	RMSE (%)	MAE (%)	
RF	0.96	3.1	2.1	0.90	3.6	2.7	0.85 ± 0.05
XGB	0.98	2.0	0.6	0.85	4.6	3.0	0.84 ± 0.03
GB	0.96	3.1	1.5	0.73	6.2	3.2	0.78 ± 0.04
DT	0.96	2.9	0.8	0.70	6.5	4.1	0.77 ± 0.06
KNN	0.58	9.5	5.2	0.72	6.2	4.4	-
LR	0.62	9.0	6.8	0.69	6.6	5.8	-

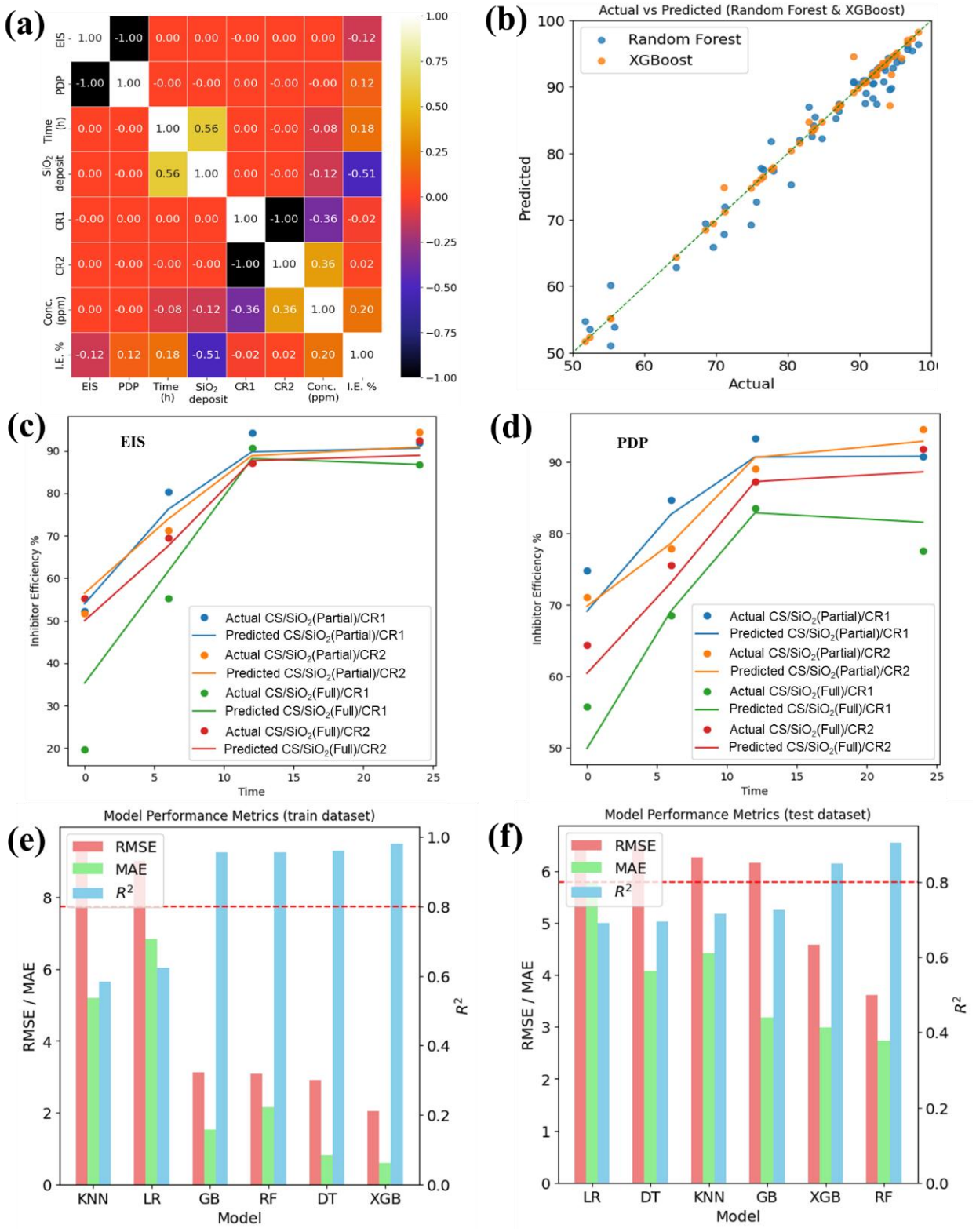

Fig. 11 (a) Correlation matrix of the entire dataset, (b) Comparison of actual vs. predicted *I.E.*% using RF and XGB regressors, (c, d) Experimental versus predicted IEs of CS/SiO_2(partial and

full)/CR1 and CS/SiO_2(partial and full)/CR1 from EIS and PDP datasets with 4-folds cross validation datasets, and (e, f) Models performance metrics of training and testing datasets.

4. Conclusions

This study assessed the effectiveness of two commercial imidazoline-based inhibitors, CRONOX-CRW85719 (CR1) and CRONOX-CRW85282 (CR2), in inhibiting interfacial corrosion on CS in simulated sour conditions (i.e., CO_2-saturated 3.5 wt.% NaCl with 1000 ppm Na_2S at 60°C), both with and without SiO_2 deposits. Concentration-dependent inhibitory efficiencies were found using EIS and PDP investigations; on clean CS surfaces, the best results were obtained at 50 ppm (CR1) and 200 ppm (CR2). Without deposits, CR1's barrier qualities were improved by its bulky molecular structure and better hydrophobicity (contact angle: 132.5° compared to 98.7° for CR2). But after 12–24 h of immersion, SiO_2 deposition (partial/full covering) significantly reduced the effectiveness of both inhibitors, lowering CR1's by 3.1–14.7% and CR2's by 0.7–4.0%. The smaller molecular architecture of CR2 allowed deeper penetration through SiO_2 pore networks, whereas CR1's bigger molecular footprint prevented interfacial access. Robust predictive measures for inhibitory effects of CR1 and CR2 were proven by machine learning validation using random forest regression (R^2 = 0.85 ± 0.05; RMSE = 3.6%; MAE = 2.7%), underscoring the crucial importance of deposit permeability and molecular shape in the design of under-deposit corrosion inhibitors. Through a combination of surface adsorption kinetics, electrochemical behavior, and machine learning modeling, the results provide a useful practical foundation for optimizing inhibitor formulations.

Associated content

Supporting Information: Plots of R_{ct} and corrosion rates against inhibitors concentrations, electrochemical impedance spectroscopy (EIS) data of samples without SiO_2 deposit, potentiodynamic polarization (PDP), EDX spectra and elemental composition, XPS wide scan, and high resolution XPS of S 2p spectra of CS with/with SiO_2 deposit in the presence of CR1 and CR2 inhibitors, LR analysis features, refitting models with P_{inh}, and LR coefficients, and RF, XGBoost and SHAP features,

Author contributions

E.M.F. contributed to experimentation, interpretation of data, and writing; **A.K.I.** contributed to experimentation, interpretation of data, and writing; **M.H.S.** contributed to experimentation, validation of data, and review; **D.A.** contributed to resources, experimentation, reviewing interpretation of data, and funding acquisition; **N.A.** contributed to experimentation, interpretation of data, and writing; **A.R.** contributed to Machine Learning Modelling, training, testing, validation, interpretation, and writing; **J.J.** contributed to machine learning algorithms data curation, interpretation, and validation; **P.K.Y.** contributed to interpretation of data, writing, and co-supervision; **A.M.A.** contributed to the conception, interpretation of data, writing, supervision and funding acquisition. All authors have given approval to the final version of the manuscript.

Acknowledgments

This publication was made possible by NPRP grant (13S-0117-200095) from the Qatar National Research Fund (QNRF) (a member of the Qatar Foundation) and Academic Research Grant (ARG01-0524-230330). Statements made herein are solely the responsibility of the authors. The authors would like to acknowledge the Central Laboratory Unit (CLU) efforts, Qatar University for SEM, EDX and elemental mapping, the Center for Advanced Materials (CAM), Qatar University for XRD analysis, and the Gas Processing Center (GPC), Qatar University for conducting the XPS analysis.

Declaration of competing interest

The authors declare no known competing financial or personal interests.

Data availability

Data will be available on request

References

[1] S. Papavinasam, R.W. Revie, A.M. Doiron, Integrity management of new pipelines: internal corrosion control, in: *NACE Corrosion*, NACE-06187 (2006).

[2] C. Kagarise, J.R. Vera, R.B. Eckert, The importance of deposit characterization in mitigating UDC and MIC in dead legs, in: *NACE Corrosion*, NACE-2017-9128 (2017).

[3] N.M. Alanazi, A. El-Sherik, A. Rasheed, S.H. Amar, M.R. Dossary, M.N. Alneemai, Corrosion of pipeline steel X-60 under field-collected sludge deposit in a simulated sour environment, *Corrosion*, **71**, 305-315 (2015).
[4] D.S. Hansen, M.V. Bram, S.M.Ø. Lauridsen, Z. Yang, Online quality measurements of total suspended solids for offshore reinjection: A review study, *Energies*, **14**, 967 (2021).
[5] I.A. Abdalsamed, I.A. Amar, F.A. Altohami, F. Salih, M. Mazek, M. Ali, A. Sharif, Corrosion strategy in oil field system, *J. Chem. Rev.*, **2**, 28-39 (2020).
[6] I.B. Obot, Under-deposit corrosion on steel pipeline surfaces: mechanism, mitigation and current challenges, *J. Bio- Tribo-Corrosion*, **7**, 49 (2021).
[7] X. Wang, R.E. Melchers, Long-term under-deposit pitting corrosion of carbon steel pipes, *Ocean Eng.*, **133**, 231-243 (2017).
[8] R. Heidersbach, Corrosion in oil and gas production, in: Microbiologically Influenced Corrosion in the Upstream Oil and Gas Industry, *CRC Press,* 3-34 (2017).
[9] Y.T. Al-Janabi, An overview of corrosion in oil and gas industry: upstream, midstream, and downstream sectors, Corrosion inhibitors in the oil and gas industry, *Chapter 1* (2020) 1-39.
[10] A. Shokri, M. Sanavi Fard, Under deposit corrosion failure: mitigation strategies and future roadmap, *Chem. Zvesti*, **77**, 1773-1790 (2023).
[11] G.A. Zhang, N. Yu, L.Y. Yang, X.P. Guo, Galvanic corrosion behavior of deposit-covered and uncovered carbon steel, *Corros. Sci.*, **86**, 202-212 (2014).
[12] Z. Wang, L. Pang, Y. Zheng, A review on under-deposit corrosion of pipelines in oil and gas fields: Testing methods, corrosion mechanisms and mitigation strategies, *Corros. Commun.*, **7**, 70-81 (2022).
[13] E.M. Suarez, L.L. Machuca, B. Kinsella, K. Lepková, CO2 Corrosion inhibitors performance at deposit-covered carbon steel and their adsorption on different deposits, *Corrosion*, **75**, 1118-1127 (2019).
[14] B. Brown, J. Moloney, 15 - Under-deposit corrosion, in: A.M. El-Sherik (Ed.) Trends in Oil and Gas Corrosion Research and Technologies, *Woodhead Publishing, Boston*, 363-383 (2017).
[15] A.A. Al-Amiery, W.K. Al-Azzawi, Organic synthesized inhibitors for corrosion protection of carbon steel: A comprehensive review, *J. Bio- Tribo-Corrosion*, **9**, 74 (2023).
[16] B.R. Fazal, T. Becker, B. Kinsella, K. Lepkova, A review of plant extracts as green corrosion inhibitors for CO2 corrosion of carbon steel, *NPJ Mater. Degrad.*, **6**, 5 (2022).

[17] Z. Shang, J. Zhu, Overview on plant extracts as green corrosion inhibitors in the oil and gas fields, *J. Mater. Res. Technol.*, **15**, 5078-5094 (2021).
[18] R.O. Medupin, K.O. Ukoba, K.O. Yoro, T.-C. Jen, Sustainable approach for corrosion control in mild steel using plant-based inhibitors: A review, *Materials Today Sustain.*, **22**, 100373 (2023).
[19] F. Kolawole, S. Kolawole, J. Agunsoye, J. Adebisi, S. Bello, S. Hassan, Mitigation of corrosion problems in API 5L steel pipeline-a review, *J. Mater. Environ. Sci*., **9**, 2397-2410 (2018).
[20] A. Groysman, Corrosion problems and solutions in oil refining and petrochemical industry, Springer, 37-99 (2017).
[21] J.K. Abaies, B.R. Odhafa, S.H. Kathim, R.A. Al-Uqaily, S.A. Al-Bayaty, Effect of inhibition on low carbon steel corrosion in acidic conditions by 2-(p-tolyl) ethylamine under different conditions, *AIP Conf. Proc.*, **070010**, 3051 (2024).
[22] M. Benoit, C. Bataillon, B. Gwinner, F. Miserque, M.E. Orazem, C.M. Sánchez-Sánchez, B. Tribollet, V. Vivier, Comparison of different methods for measuring the passive film thickness on metals, *Electrochim. Acta,* **201**, 340-347 (2016).
[23] V. Pandarinathan, K. Lepková, S.I. Bailey, R. Gubner, Evaluation of corrosion inhibition at sand-deposited carbon steel in CO2-saturated brine, *Corros. Sci.*, **72**, 108-117 (2013).
[24] B. Fan, H. Zhu, H. Li, H. Tian, B. Yang, Penetration of imidazoline derivatives through deposited scale for inhibiting the under-deposit corrosion of pipeline steel, *Corros. Sci.*, **235**, 112209 (2024).
[25] J. Song, J. Zhang, C. Wang, M. Ge, Study on the inhibition mechanism of corrosion under inert deposit-covered X65 steel by three corrosion inhibitors, *Surf. Coat. Technol.,* **484**, 130805 (2024).
[26] R. Li, X. Wang, J. Chen, Y. Wang, Understanding of ammonium salts under-deposit corrosion: Electrochemical and AIMD investigations, *Corros. Sci.*, **229**, 111887 (2024).
[27] C. Verma, A.H. Al-Moubaraki, A. Alfantazi, K.Y. Rhee, Heterocyclic amino acids-based green and sustainable corrosion inhibitors: Adsorption, bonding and corrosion control, *J. Clean. Prod.*, **446**, 141186 (2024).
[28] C. Verma, D.K. Verma, E.E. Ebenso, M.A. Quraishi, Sulfur and phosphorus heteroatom-containing compounds as corrosion inhibitors: An overview, *Heteroat. Chem.*, **29**, e21437 (2018).

[29] E.D. Akpan, A. Kumar Singh, H. Lgaz, T.W. Quadri, S. Kumar Shukla, B. Mangla, A. Dwivedi, O. Dagdag, Sheetal, E. Edem Inyang, E.E. Ebenso, Coordination compounds as corrosion inhibitors of metals: A review, *Coord. Chem. Rev.*, **499**, 215503 (2024).

[30] H. Lin, X. Chen, Z. Luo, J. Xu, P. Lu, T. Xie, J. Tang, H. Wang, Corrosion Inhibition Properties of Corrosion Inhibitors to under-Deposit Corrosion of X65 Steel in CO2 Corrosion Conditions, *Molecules*, **29**, 2611 (2024).

[31] B. Anandkumar, N.G. Krishna, R.V. Solomon, T. Nandakumar, J. Philip, Synergistic enhancement of corrosion protection of carbon steels using corrosion inhibitors and biocides: Molecular adsorption studies, DFT calculations and long-term corrosion performance evaluation, *J. Environ. Chem. Eng.*, **11**, 109842 (2023).

[32] E.M. Fayyad, M.H. Sliem, N. Al-Qahtani, M.P. Ryan, A.M. Abdullah, Assessing underdeposit corrosion inhibitor performance for carbon steel in CO2/Sulfide environment, *J. Mater. Res. Technol.*, **28**, 1433-1451 (2024).

[33] K.T. Butler, D.W. Davies, H. Cartwright, O. Isayev, A. Walsh, Machine learning for molecular and materials science, *Nature*, **559**, 547-555 (2018).

[34] L.B. Coelho, D. Zhang, Y. Van Ingelgem, D. Steckelmacher, A. Nowé, H. Terryn, Reviewing machine learning of corrosion prediction in a data-oriented perspective, *NPJ Mater. Degrad.*, **6**, 8 (2022).

[35] A. Chen, X. Zhang, Z. Zhou, Machine learning: accelerating materials development for energy storage and conversion, *InfoMat*, **2**, 553-576 (2020).

[36] Y. Diao, L. Yan, K. Gao, Improvement of the machine learning-based corrosion rate prediction model through the optimization of input features, *Mater. Des*., **198**, 109326 (2021).

[37] L. Yan, Y. Diao, Z. Lang, K. Gao, Corrosion rate prediction and influencing factors evaluation of low-alloy steels in marine atmosphere using machine learning approach, *Sci. Technol. Adv. Mater.*, **21**, 359-370 (2020).

[38] A. Roy, M. Taufique, H. Khakurel, R. Devanathan, D.D. Johnson, G. Balasubramanian, Machine-learning-guided descriptor selection for predicting corrosion resistance in multi-principal element alloys, *NPJ Mater. Degrad.*, **6**, 9 (2022).

[39] T. Sutojo, S. Rustad, M. Akrom, A. Syukur, G.F. Shidik, H.K. Dipojono, A machine learning approach for corrosion small datasets, *NPJ Mater. Degrad.*, **7**, 18 (2023).

[40] C. Özkan, L. Sahlmann, C. Feiler, M. Zheludkevich, S. Lamaka, P. Sewlikar, A. Kooijman, P. Taheri, A. Mol, Laying the experimental foundation for corrosion inhibitor discovery through machine learning, *NPJ Mater. Degrad.*, **8**, 21 (2024).

[41] D.A. Winkler, Predicting the performance of organic corrosion inhibitors, *Metals*, **7**, 553 (2017).

[42] T.H. Pham, P.K. Le, A data-driven QSPR model for screening organic corrosion inhibitors for carbon steel using machine learning techniques, *RSC Adv.*, **14** , 11157-11168 (2024).

[43] M. Aghaaminiha, R. Mehrani, M. Colahan, B. Brown, M. Singer, S. Nesic, S.M. Vargas, S. Sharma, Machine learning modeling of time-dependent corrosion rates of carbon steel in presence of corrosion inhibitors, *Corros. Sci.*, **193**, 109904 (2021).

[44] A.K. Ipadeola, K. Eid, A.M. Abdullah, R.S. Al-Hajri, K.I. Ozoemena, Pd/Ni-metal–organic framework-derived porous carbon nanosheets for efficient CO oxidation over a wide pH range, *Nanoscale Adv.*, **4**, 5044-5055 (2022).

[45] A.K. Ipadeola, A.B. Haruna, A.M. Abdullah, M.F. Shibl, D. Ahmadaliev, K.I. Ozoemena, K. Eid, Electrocatalytic CO oxidation on porous ternary PdNiO-CeO2/carbon black nanocatalysts: Effect of supports and electrolytes, *Catal. Today*, **421**, 114178 (2023).

[46] A.K. Ipadeola, A.B. Haruna, A.M. Abdullah, R.S. Al-Hajri, R. Viter, K.I. Ozoemena, K. Eid, Ternary PdNiO nanocrystals-ornamented porous CeO 2/onion-like carbon for electrooxidation of carbon monoxide: unveiling the effect of supports and electrolytes, *Catal. Sci. Technol.*, **13**, 3035-3046 (2023).

[47] D.I. Njoku, I. Ukaga, O.B. Ikenna, E.E. Oguzie, K.L. Oguzie, N. Ibisi, Natural products for materials protection: corrosion protection of aluminium in hydrochloric acid by Kola nitida extract, *J. Mol. Liq.*, **219**, 417-424 (2016).

[48] S. Bashir, H. Lgaz, I.-M. Chung, A. Kumar, Potential of Venlafaxine in the inhibition of mild steel corrosion in HCl: insights from experimental and computational studies, *Chemical Zvesti*, **73**, 2255-2264 (2019).

[49] M.H. Sliem, M. Afifi, A. Bahgat Radwan, E.M. Fayyad, M.F. Shibl, F.E.-T. Heakal, A.M. Abdullah, AEO7 surfactant as an eco-friendly corrosion inhibitor for carbon steel in HCl solution, *Sci. Rep.*, **9**, 2319 (2019).

[50] O. Kaczerewska, R. Leiva-Garcia, R. Akid, B. Brycki, I. Kowalczyk, T. Pospieszny, Effectiveness of O-bridged cationic gemini surfactants as corrosion inhibitors for stainless steel in 3 M HCl: Experimental and theoretical studies, *J. Mol. Liq.,* **249**, 1113-1124 (2018).
[51] U. Angst, M. Büchler, On the applicability of the Stern–Geary relationship to determine instantaneous corrosion rates in macro-cell corrosion, *Mater. Corros.*, **66**, 1017-1028 (2015).
[52] M. Damej, S. Skal, J. Aslam, M. Zouarhi, H. Erramli, A.A. Alrashdi, H.-S. Lee, H. Lgaz, An environmentally friendly formulation based on Cannabis sativa L. seed oil for corrosion inhibition of E24 steel in HCl medium: Experimental and theoretical study, *Colloids Surf. A Physicochem. Eng. Asp.*, **643**, 128745 (2022).
[53] P.D. Desai, C.B. Pawar, M.S. Avhad, A.P. More, Corrosion inhibitors for carbon steel: A review, *Vietnam J. Chem.*, **61**, 15-42 (2023).
[54] A.K. Ipadeola, A. Abdelgawad, B. Salah, A.M. Abdullah, K. Eid, Interfacial Engineering of Porous Pd/M (M = Au, Cu, Mn) Sponge-like Nanocrystals with a Clean Surface for Enhanced Alkaline Electrochemical Oxidation of Ethanol, *Langmuir,* **39**, 13830-13840 (2023).
[55] P.S. Abdar, M.B. Hariri, A. Kahyarian, S. Nesic, A revision of mechanistic modeling of mild steel corrosion in H2S environments, *Electrochim. Acta*, **382**, 138231 (2021).
[56] A.A. Fadhil, A.A. Khadom, H. Liu, C. Fu, J. Wang, N.A. Fadhil, H.B. Mahood, (S)-6-Phenyl-2, 3, 5, 6-tetrahydroimidazo [2, 1-b] thiazole hydrochloride as corrosion inhibitor of steel in acidic solution: Gravimetrical, electrochemical, surface morphology and theoretical simulation, *J. Mol. Liq.*, **276**, 503-518 (2019).
[57] A.K. Ipadeola, N.Z. Lisa Mathebula, M.V. Pagliaro, H.A. Miller, F. Vizza, V. Davies, Q. Jia, F. Marken, K.I. Ozoemena, Unmasking the latent passivating roles of Ni (OH) 2 on the performance of Pd–Ni electrocatalysts for alkaline ethanol fuel cells, *ACS Appl. Energy Mater.*, **3**, 8786-8802 (2020).
[58] B. Salah, A.K. Ipadeola, A. Khan, Q. Lu, Y. Ibrahim, E.L. Darboe, A.M. Abdullah, K. Eid, Unveiling the electrochemical CO oxidation activity on support-free porous PdM (M = Fe, Co, Ni) foam-like nanocrystals over a wide pH range, *Energy Convers. Manag. X*, **20**, 100449 (2023).
[59] Y.I. Kuznetsov, G.V. Redkina, Thin Protective Coatings on Metals Formed by Organic Corrosion Inhibitors in Neutral Media, *Coatings*, **12**, 149 (2022).
[60] V. Maurice, P. Marcus, Current developments of nanoscale insight into corrosion protection by passive oxide films, *Curr. Opin. Solid State Mater. Sci.*, **22**, 156-167 (2018).

[61] R.N. Goswami, R. Saini, S. Mehta, G. Verma, A. Ray, O.P. Khatri, Ti3C2Tx MXene-Polyaniline Nanocomposites for Redesigning Epoxy Coatings to Improve Anticorrosive Performance, *ACS Appl. Eng. Mater.*, **2**, 1396-1410 (2024).

[62] Y. Zhang, Q. Wang, C.S. Ramachandran, P. Guo, A. Wang, Microstructure and Performance of High-Velocity Oxygen-Fuel Coupled Physical Vapor Deposition (HVOF-PVD) Duplex Protective Coatings: A Review, *Coatings,* **12**, 1395 (2022).

[63] G. Ruhi, H. Bhandari, S.K. Dhawan, Designing of corrosion resistant epoxy coatings embedded with polypyrrole/SiO2 composite, *Prog. Org. Coat.*, **77**, 1484-1498 (2014).

[64] A. Dehghani, G. Bahlakeh, B. Ramezanzadeh, M. Ramezanzadeh, Potential role of a novel green eco-friendly inhibitor in corrosion inhibition of mild steel in HCl solution: Detailed macro/micro-scale experimental and computational explorations, *Constr. Build Mater.*, **245**, 118464 (2020).

[65] Q. Fang, Y. Zhao, J. Wei, Z. Wang, J. Yao, Investigation of the Working Mechanism of CO2–H2O Flow Corrosion of Mild Carbon Steel, *Ind. Eng. Chem. Res.*, **63**, 636-647 (2024).

[66] A.A. Fadhil, A.A. Khadom, H. Liu, C. Fu, J. Wang, N.A. Fadhil, H.B. Mahood, (S)-6-Phenyl-2,3,5,6-tetrahydroimidazo[2,1-b] thiazole hydrochloride as corrosion inhibitor of steel in acidic solution: Gravimetrical, electrochemical, surface morphology and theoretical simulation, *J. Mol. Liq.,* **276**, 503-518 (2019).

[67] I.A.W. Ma, S. Ammar, S.S.A. Kumar, K. Ramesh, S. Ramesh, A concise review on corrosion inhibitors: types, mechanisms and electrochemical evaluation studies, *J. Coat. Technol. Res.*, **19**, 241-268 (2022).

[68] N.D. Nam, P.V. Hien, N.T. Hoai, V.T.H. Thu, A study on the mixed corrosion inhibitor with a dominant cathodic inhibitor for mild steel in aqueous chloride solution, *J. Taiwan Inst. Chem. Eng.,* **91**, 556-569 (2018).

[69] L.L. Machuca, K. Lepkova, A. Petroski, Corrosion of carbon steel in the presence of oilfield deposit and thiosulphate-reducing bacteria in CO2 environment, *Corros. Sci.*, **129**, 16-25 (2017).

[70] L. Pang, Z.B. Wang, M.H. Lu, Y. Lu, X. Liu, Y.G. Zheng, Inhibition performance of benzimidazole derivatives with different heteroatoms on the under-deposit corrosion of carbon steel in CO2-saturated solution, *Corros. Sci.*, **192**, 109841 (2021).

[71] T. Liang, H. Yuan, C. Li, S. Dong, C. Zhang, G. Cao, Y. Fan, X. Zhao, X. Cao, Corrosion inhibition effect of nano–SiO2 for galvanized steel superhydrophobic surface, *Surf. Coat. Technol.*, **406**, 126673 (2021).

[72] J. Kvarekvål, G. Svenningsen, Effect of High H2S Partial Pressures on Localized Corrosion of Carbon Steel, *NACE Corrosion*, **2015**, NACE-2015-5720 (2015).

[73] M. Askari, M. Aliofkhazraei, S. Afroukhteh, A comprehensive review on internal corrosion and cracking of oil and gas pipelines, *J. Nat. Gas Sci. Eng.*, **71**, 102971 (2019).

[74] Y. He, W.T. Sun, S.C. Wang, P.A.S. Reed, F.C. Walsh, An electrodeposited Ni-P-WS2 coating with combined super-hydrophobicity and self-lubricating properties, *Electrochim. Acta*, **245**, 872-882 (2017).

[75] Z.B. Wang, L. Pang, Y.G. Zheng, A review on under-deposit corrosion of pipelines in oil and gas fields: Testing methods, corrosion mechanisms and mitigation strategies, *Corros. Commun.*, **7**, 70-81 (2022).

[76] D. Csákberényi-Malasics, J.D. Rodriguez-Blanco, V.K. Kis, A. Rečnik, L.G. Benning, M. Pósfai, Structural properties and transformations of precipitated FeS, *Chem. Geol.*, **294-295**, 249-258 (2012).

[77] S.A. Zakaria, K. Motham, A.S. Anasyida, H. Zuhailawati, M.H. Hassan, B.K. Dhindaw, Microstructure, Mechanical Properties, and Corrosion Behaviour of Cryorolled Low-Carbon Steel at Different Thickness Reductions, *JOM*, **75**, 3900-3910 (2023).

[78] A. Grosvenor, B. Kobe, M.C. Biesinger, N. McIntyre, Investigation of multiplet splitting of Fe 2p XPS spectra and bonding in iron compounds, *Surf. Interface Anal.*, **36**, 1564-1574 (2004).

[79] S. Zhang, Q. Lu, H. Zhang, K. Liang, Y. Tan, C. Sun, Shifts in the Binding Energies of Cr2p, Fe2p and O1s electrons of Alloy Oxide Films in the Presence of Pb During High-Temperature Water Corrosion, *Int. J. Electrochem. Sci.*, **15**, 1853-1860 (2020).

[80] T.K. Ekanayaka, H. Kurz, K.A. McElveen, G. Hao, E. Mishra, R.Y. Lai, B. Weber, P.A. Dowben, Evidence for surface effects on the intermolecular interactions in Fe (II) spin crossover coordination polymers, Phys. *Chem. Chem. Phys.*, **24**, 883-894 (2022).

[81] C. Verma, H. Lgaz, D.K. Verma, E.E. Ebenso, I. Bahadur, M.A. Quraishi, Molecular dynamics and Monte Carlo simulations as powerful tools for study of interfacial adsorption behavior of corrosion inhibitors in aqueous phase: A review, *J. Mol. Liq.,* **260**, 99-120 (2018).

[82] L. Guo, I.B. Obot, X. Zheng, X. Shen, Y. Qiang, S. Kaya, C. Kaya, Theoretical insight into an empirical rule about organic corrosion inhibitors containing nitrogen, oxygen, and sulfur atoms, *Appl. Surf. Sci.*, **406**, 301-306 (2017).
[83] T. Chen, C. Guestrin, Xgboost: A scalable tree boosting system, in: Proceedings of the 22nd acm sigkdd international conference on knowledge discovery and data mining, 785-794 (2016).
[84] C. Wade, K. Glynn, Hands-On Gradient Boosting with XGBoost and scikit-learn: Perform accessible machine learning and extreme gradient boosting with Python, Packt Publishing Ltd, (2020).
[85] D.A. Winkler, A.E. Hughes, C. Özkan, A. Mol, T. Würger, C. Feiler, D. Zhang, S.V. Lamaka, Impact of inhibition mechanisms, automation, and computational models on the discovery of organic corrosion inhibitors, *Prog. Mater. Sci.*, **149**, 101392 (2025).